The Formation of Type B CAIs: Evolution from Type A CAIs

G. J. MacPherson[1], A. N. Krot[2], N. T. Kita[3], E. S. Bullock[4], K. Nagashima[2], T. Ushikubo[3,5], M. A. Ivanova[1,6]

[1] Dept. of Mineral Sciences, Museum of Natural History, Smithsonian Institution, Washington, DC, USA 20560

[2] Hawai'i Institute of Geophysics and Planetology, School of Ocean and Earth Science and Technology, University of Hawaiʻi at Mānoa, Honolulu, HI 96822, USA

[3] WiscSIMS, Department of Geoscience, University of Wisconsin-Madison, Madison, WI 53706

[4] Carnegie Institution for Science, Earth and Planets Laboratory, 5241 Broad Branch Rd., N.W., Washington, DC 20015 USA

[5] Kochi Institute for Core Sample Research, JAMSTEC, Nankoku, Kochi 783-8502 Japan.

[6] Vernadsky Institute, Kosygin St. 19, Moscow, Russia

Submitted to: *Geochimica et Cosmochimica Acta* July 21, 2021

Revised version submitted December 22, 2021.

ABSTRACT

Five Type A CAIs from three CV3 chondrites (Vigarano, Northwest Africa 3118, Allende), which differ in age by no more than ~10^5 years, show mineralogical and textural evidence of gradual transition into Type Bs, indicating that Type B inclusions formed by evolution of Type A CAIs in the solar nebula. This model differs from the conventional condensation model in which aggregates of condensate grains form different kinds of CAIs depending on the relative populations of different kinds of grains. In our model the

pyroxene forms nearly isochemically by reaction of perovskite with melilite under highly reducing conditions, and the reaction may be triggered by influx of hydrogen from the gas. Anorthite requires the addition of silica from the gas, and originally forms as veins and reaction rims on gehlenitic melilite within Fluffy Type As. Later partial re-melting of these assemblages results in the formation of poikilitic pyroxene and anorthite that enclose rounded (partially melted) tablets of melilite. Oxygen isotopes in four of the CAIs support the formation of Ti-rich ^{16}O-depleted pyroxene from ^{16}O-depleted perovskite, but not in the fifth CAI. An alternative possibility is that Ti-rich ^{16}O-depleted pyroxene is the result of later solid-state exchange that preferentially affects the most Ti-rich pyroxene. Regardless of the origin of the ^{16}O-depleted pyroxene, we give a model for nebular reservoir evolution based on sporadic FU-Orionis flare-ups in which the ^{16}O-rich region near the proto-Sun fluctuated in size depending on whether the proto-Sun was in flare-up stage or quiescent.

INTRODUCTION

Grossman (1975) classified the large silicate-rich calcium-aluminum-rich inclusions (CAIs) in Allende, now extended to all CV3s, into three varieties based on their mineralogy: Type As that contain mostly melilite with lesser amounts of spinel and Ti-rich clinopyroxene; Type Bs that contain subequal amounts of melilite, Ti-rich clinopyroxene, anorthite, and spinel; and Type I (for intermediate) that have similar mineralogy to Type B but whose pyroxene is intermediate in composition to that in Types A or B. Type I is now known as Type C. Subsequent work demonstrated that the three CAI varieties differ in bulk chemistry as well, although they do form a continuum (Beckett, 1986; Simon and Grossman, 2004), and that Type C ("I") are in no way intermediate between Types A and B (Beckett, 1986; Wark, 1987; MacPherson and Huss, 2005).

Of the three varieties, the Type Bs are the best known, yet their origins are not well understood. In terms of size and mineralogy, they have no counterparts in any other type of chondrite other than CVs and CKs. All Type Bs solidified from melt droplets, which is not unusual, but unlike Type As and virtually every other kind of CAI, there are no un-melted aggregates equivalent to a Type B. Among other differences, Type Bs differ from Type As in containing abundant primary (igneous) anorthite, which means that Type Bs are more silica-rich than Type As. Yet, there is a continuum of bulk compositions between Type Bs and Type As (Beckett, 1986; Simon and Grossman, 2004; Ivanova et al., 2021).

Much has been written about the igneous history of Type Bs (MacPherson and Grossman, 1981; Stolper, 1982; Stolper and Paque, 1986), and about how the bulk compositions of Type Bs deviate systematically away from the bulk compositions of equilibrium condensates out of a hot solar gas

(Grossman et al., 2000; Richter et al., 2002, 2007). Very little has been written about the precursors to the once-molten objects that we now observe. The general assumption is that Type Bs were melted from aggregates of primary condensate grains, themselves the product of equilibrium condensation (e.g., Yoneda and Grossman, 1995), with varying degrees of melt evaporation that modified the bulk chemical and isotopic compositions (e.g., Grossman et al., 2000; Richter et al., 2002, 2007). In this view, Type A CAIs sampled higher temperature aggregate assemblages than did either Types B or C (anorthite-rich) CAIs, which aggregated at lower temperatures. Yet if Compact Type As formed by melting of Type A aggregates ("Fluffy Type As), from what did the Type Bs melt? There is no such thing as a "Fluffy"[1] Type B, which argues against this simple model. One paper that specifically did address the question of Type B precursors is Lin and Kimura (2003), who measured the bulk compositions of Type A CAIs in the Ningqiang CV chondrite and showed that they overlap with those of Type B CAIs. Their model, which is distinct from ours in several respects, is discussed later.

In this paper, we argue that Type Bs evolved from Type As owing to continued interactions with the surrounding nebular gas during repeated episodes of reheating and melting. In this model, the key to understanding Type B CAIs lies in studying and understanding Type As, especially the evolution of Fluffy Type As to Compact Type As.

As a result of our recent detailed studies of numerous Type A CAIs from the reduced CV3 chondrites (Vigarano, Efremovka, Leoville, and Northwest Africa (NWA) 3118), petrologic patterns have begun to emerge that allow us for the first time to see how pyroxene and anorthite first begin to form and grow in Type A CAIs, leading eventually into transitional Type A/B CAIs and ultimately Type Bs. The formation mechanisms of pyroxene and anorthite in CAIs are different; specifically, anorthite requires the addition of silicon to a Type A bulk composition whereas pyroxene, as we will show below, can form nearly isochemically.

This paper documents how pyroxene and anorthite first began to form in FTAs and CTAs, with constraints provided by oxygen isotopes in the context of detailed petrographic and petrologic analysis. Although the features described herein occur in many similar CAIs, our observations and interpretations are based on five especially illustrative inclusions. Also, because the textural observations are integral with the mineral chemistry and isotopic measurements, we will treat each CAI in its entirety before treating the next CAI. The results presented herein were first reported by MacPherson et al. (2012a).

The inclusions studied here in were part of a much larger study of the high-precision Al Mg isotopic systematics of Type A CAIs. Over the course of that study, we began to recognize the patterns described in this paper. These particular CAIs were chosen to be the most representative of the features of interest. Several of the inclusions are unusual for their types, being transitional between Types A and B, and it is precisely those transitional features that are instructive. The Al Mg isotopic compositions of these objects, although not pivotal to the model for how Type Bs form, are important to the story because they show that all of the CAIs formed within a relatively restricted time period, on the order of 10^5 years (given the usual assumption about nebular homogeneity in terms of the initial ^{26}Al/^{27}Al ratio).

ANALYTICAL TECHNIQUES

High-resolution backscattered electron (BSE) images and x-ray element distribution maps of polished sections were obtained using the FEI NOVA NanoSEM 600 scanning electron microscope (SEM) at the Smithsonian Institution, operated at 15 kV with a sample current of 2−3 nA. The SEM is equipped with a Thermo-Noran energy dispersive x-ray analytical system, and data are processed using Thermo-Scientific Noran System Six software.

Mineral compositions were measured with a JEOL JXA-8900 automated five-spectrometer wavelength-dispersive electron microprobe at the Smithsonian Institution, operated at 15 kV, 15−20 nA beam current, and counting times in the range of 10−40 seconds (depending on the element).

Oxygen isotopic measurements in four CAIs were done in situ with the Cameca IMS-1280 ion microprobe at the University of Hawai‘i (UH) using three analytical protocols. For coarse grains in CAIs *1N-b* and *16N* from NWA 3118, *TS19-F1* from Allende, and *3138-F8* from Vigarano, we used the protocol described in Nagashima et al. (2015). A ~1.2 nA Cs$^+$ primary ion beam was focused and rastered over 7×7 μm. The ion microprobe was operated at –10 kV with a 50 eV energy window. Secondary ions of ^{16}O$^-$ and ^{18}O$^-$ were measured on Faraday cups (FCs) and ^{17}O$^-$ was measured on the axial electron multiplier (EM). The mass resolving power (m/Δm) for ^{16}O$^-$ and ^{18}O$^-$ was ~2000, and that for ^{17}O$^-$ was ~5500, sufficient to separate interfering ^{16}OH$^-$. Small grains (<10 μm) in *TS19-F1* and *3138-F8* were measured using a different protocol, with a ~30 pA primary beam focused to ~1-2 μm. The grains to be measured were marked with a focused electron beam following a technique described in Nagashima et al. (2015). Three oxygen isotopes were measured

---

[1] We use the term “Fluffy” (e.g. Fluffy Type A; FTA) to refer to an aggregate object that did not experience significant melting, although some sintering is likely. In contrast, Compact Type A (CTA) CAIs did melt to some degree. The term Fluffy Type A is used herein somewhat differently than as originally proposed by MacPherson and Grossman (1984) in that we do not assume that the aggregates consist of pristine primary condensate crystals.

simultaneously: $^{16}O^-$ was measured on a FC and $^{17}O^-$ and $^{18}O^-$ were measured on EMs. The mass resolving power for $^{16}O^-$ and $^{18}O^-$ was ~2000, and that for $^{17}O^-$ was ~5500. Finally, small grains in *3138-F8* were measured with a ~250 pA primary beam rastered over 5×5 μm. $^{16}O^-$ and $^{17}O^-$ were measured simultaneously on a FC and the axial EM, followed by $^{18}O^-$ measurement on the axial EM. The mass resolving power for $^{16}O^-$ was ~2000, and that for $^{17}O^-$ and $^{18}O^-$ was ~5500.

Instrumental fractionation was corrected using terrestrial standards including San Carlos olivine (for gehlenitic melilite), Cr-diopside (for Al-Ti-diopside), Burma spinel (for spinel and hibonite, and perovskite in *16N* and *3138-F8*), Miyake-jima anorthite (for anorthite), and perovskite (for perovskite in TS19). After SIMS measurements, the spots analyzed for oxygen isotopes were verified with secondary and BSE images using SEMs at UH and the Smithsonian Institution. Oxygen-isotope compositions are reported as $\delta^{17}O$ and $\delta^{18}O$, deviations from Vienna Standard Mean Ocean Water (VSMOW; $^{17}O/^{16}O_{VSMOW} = 0.00038288$; $^{18}O/^{16}O_{VSMOW} = 0.0020052$) in parts per thousand: $d^{17,18}O_{VSMOW} = [(^{17,18}O/^{16}O_{sample}) / (^{17,18}O/^{16}O_{VSMOW}) - 1] \times 1000$, and as deviation from the terrestrial fractionation (TF) line, $\Delta^{17}O$ (see below). Typical uncertainties for $\delta^{17}O$, $\delta^{18}O$, and $\Delta^{17}O$ were ~0.8, 1.0, 1.8‰, ~1.3, 2.0, ~2.0‰, and ~1.3, 1.6, and 2.0‰, for the 1st, 2nd and 3rd protocols, respectively.

Because the characteristic oxygen isotopic property of CAIs is enrichment in ^{16}O, a useful shorthand notation for enrichment or depletion in ^{16}O is to report the data as $\Delta^{17}O$ (graphically, the vertical distance above or below the terrestrial fractionation line):

$$\Delta^{17}O = \delta^{17}O - 0.52 \times \delta^{18}O \quad (1)$$

In addition to spot analyses, we obtained oxygen isotope maps ($\delta^{18}O$ isotopographs) for several regions in the CAIs using a technique described in Nagashima et al. (2015) with the UH isotope microscope system consisting of the two-dimensional solid-state SCAPS (Stacked CMOS type Active Pixel Sensor) ion detector (Yurimoto et al., 2003) attached to the Cameca ims-1280.

All magnesium isotopic analyses were acquired using the Cameca IMS-1280 at the University of Wisconsin-Madison (WiscSIMS), utilizing multi-collection (MC) Faraday cups (FC) for all phases except anorthite, which was analyzed using mono-collection electron multiplier (EM) analyses under conditions similar to those given in Kita et al. (2012). For MCFC analyses, the primary O^- ion beam was adjusted to the 20μm × 25μm oval shapes with an intensity of 7 nA (spinel) and 22 nA (melilite and fassaite). The 22 nA primary beam resulted in light sputtering of surrounding areas ~35 μm across due to aberration of primary column (Kita et al. 2012). Secondary $^{24}Mg^+$ions intensities were at the range of $(0.1-3) \times 10^8$ cps, depending on the major element compositions. Each analysis took 8 minutes. The baseline of the FC detectors was monitored during presputtering and averaged over 8 analyses. Due to the differences in Mg secondary intensities, we ran each mineral separately. A melilite glass standard (~Ak_{67}), a fassaite glass standard with 5 wt.% TiO_2, and a natural spinel standard were used as running standards for melilite, fassaite, spinel and olivine analysis, respectively. We also measured several melilite glass standards ($Åk_{15}$−$Åk_{65}$) and fassaite glass standards with various TiO_2 contents (2–10%) that were used to estimate instrumental bias corrections (see supplemental files). A total of 8 sets of standard analyses were obtained by bracketing 4−10 unknown sample analyses and the average of 8 standard analyses were used to correct instrumental bias on the measured Mg isotope ratios.

The isotope mass fractionation correction (both instrumental and natural) is applied to measured Mg isotope ratios to estimate excess ^{26}Mg. The fractionation-corrected δ^{26}Mg* values were calculated using an exponential law with slope of 0.5128 from the evaporation experiment of Davis et al. (2015). Both internal errors and the external reproducibility of fractionation corrected δ^{26}Mg* values for standards were typically 0.04–0.08‰ (2SD) for fassaite glass and spinel standards and 0.06–0.20‰ (2SD) for $Åk_{65}$–$Åk_{15}$ glass standard. The external reproducibilities of bracket standards were propagated to the uncertainties of δ^{26}Mg* values of the sample analyses. The reproducibility of the measured ^{27}Al/^{24}Mg ratios of the running standard was better than 1% (2SD) for melilite, spinel, and fassaite glass and mineral standards. Relative sensitivity factors (RSF) were determined by using ^{27}Al/^{24}Mg ratios of these standards determined by electron microprobe (Kita et al. 2012). Final uncertainties include propagated uncertainties of individual CAI mineral analyses and that of the RSFs (~1%). We applied an additional 10% correction to the fassaite RSF, because we previously observed 10% offsets between the fassaite glass standard and natural CAI pyroxenes that are homogeneous in major element compositions.

For mono-collection electron multiplier (EM) analyses in pulse counting mode, the primary O^- ion beam was adjusted to the oval shape with 4μm × 6μm diameter with the intensity of 24 pA for anorthite analyses similar to the condition in Ushikubo et al. (2017). Anorthite glass standards with a range of MgO contents (0.1, 0.5, 1.0%, Kita et al., 2012) were analyzed in order to correct instrumental biases for Mg isotopes and ^{27}Al/^{24}Mg RSF. The intensity of ^{24}Mg$^+$ ions was typically at 3 × 10^{4}cps and (2-6) × 10^3 cps for anorthite glass standard with 1.0% MgO and CAI anorthite, respectively. A single analysis consists of 200-300 cycles of collecting Mg and Al isotope signals, which takes 2-3 hours. Typical precisions of δ^{26}Mg* were 1-2‰ for 0.5-1% MgO anorthite glass standards, 4‰ for 0.1% MgO anorthite glass standard, and 3-8‰ for anorthite in CAIs. The external reproducibility of the RSF for the anorthite standard was ~1.5%, which was propagated to final uncertainties in the ^{27}Al/^{24}Mg ratios

The data are plotted graphically as δ^{26}Mg* *vs.* ^{27}Al/^{24}Mg, where

$$\delta^{26}\text{Mg}^* = \delta^{26}\text{Mg} - \left[\left(\frac{\delta^{25}\text{Mg}}{1000}+1\right)^{1/\beta} - 1\right]\times 1000 \qquad (2)$$

We adopt β =0.5128 from Davis et al. (2015) for both natural and instrumental mass dependent fractionation. A detailed description of the data reduction scheme was reported in EA1 of Ushikubo et al. (2017) (see supplemental data). For mono-collection EM data, instrumental fractionation was corrected by using β = 0.514 during analysis (Kita et al. 2012), because low precision Mg isotope data are insensitive to differences in β.

All isochron slopes reported in this paper were calculated using ISOPLOT Model 1 fits (Ludwig, 2003).

RESULTS

Vigarano 3138-F8 (Fig. 1; hereafter, *3138-F8*) was described briefly by MacPherson et al. (2012b). It is an irregularly shaped FTA CAI, approximately 1.8 × 4.8 mm in overall size, consisting mostly of melilite plus abundant hibonite and spinel, with lesser Ti-rich pyroxene and perovskite. The inclusion contains only traces of sodium-rich secondary alteration phases. It is heavily fractured and much of the outer edge of the CAI appears to be fracture surfaces, but locally a Wark-Lovering (WL) rim sequence (Wark and Lovering, 1977) is preserved. This rim is variable in its structure: In some places the layers include aluminous diopside, anorthite, and spinel but in most places the spinel layer is missing and only anorthite and pyroxene are present. There is no perovskite in the rim sequence. Melilite in *3138-F8* is uniformly aluminous, with an overall composition range Åk$_{0\text{–}23}$ and mostly in the range Åk$_{8\text{–}20}$. The most Al-rich melilite (Åk$_{0\text{–}10}$) consistently is located in two petrographic contexts: (1) directly underlying the WL rim, and (2) immediately adjacent to hibonite crystals. Pyroxene in *3138-F8* occurs in two compositional varieties. Aluminous diopside occurs in the WL rim (and faulted inliers of the rim that are present in the CAI interior), and highly Ti-rich pyroxene occurring as small regions within the CAI interior that enclose perovskite (Fig. 2). Whereas the rim pyroxene contains only several percent TiO_2 at most (calculating all Ti as Ti^{4+}), the interior pyroxene uniformly contains 15–19 wt.% TiO_2 of which about 65% on average is trivalent (here and following, based on stoichiometric calculations of structural formulae). Hibonite in *3138-F8* is Ti-rich, 6.5–8.6 wt.% TiO_2, and contains 3.3–4.5 wt.% MgO. Spinel is close to end-member $MgAl_2O_4$ with minor amounts of CaO and SiO_2. Spinel near the WL rim sequence can contain several wt.% FeO.

Figure 3 shows the oxygen-isotope composition of individual minerals in *3138-F8*. The data are unusual in several ways. First, in contrast with most Allende CAIs, the melilite in *3138- F8* is not uniformly ^{16}O-depleted (Δ^{17}O ranges from ~ −11 to ~ −5‰). This has been observed previously in other CV3 CAIs by other workers (e.g., Yurimoto et al., 1998), but it is uncommon. In fact, none of the melilite analyses plot near the intersection of the Carbonaceous Chondrite Anhydrous Mineral (CCAM) line with the Terrestrial Fractionation (TF) line. The most ^{16}O-rich melilites invariably are in the outer parts of the inclusion, particularly near the WL rim. The most ^{16}O-depleted pyroxenes (Δ^{17}O ~ −3‰) occur in the CAI core; the pyroxenes are Ti-rich and enclose irregularly shaped perovskite grains. Titanium-poor Al-diopside in the WL rim sequence is, by contrast, very ^{16}O-enriched (Δ^{17}O ~ −22‰), similar to spinel and hibonite in the CAI interior. Perovskite in *3138-F8* is the most ^{16}O-depleted phase (Δ^{17}O ~ −1‰). Although the lone perovskite data point shown plots near many of the melilite points, SEM examination of the ion pit following analysis showed that the spot has about 20% overlap with a neighboring spinel grain. Subtraction of 20% of the average spinel oxygen isotopic composition from the perovskite composition puts pure perovskite up near the top of the CCAM line, next to the analyses of pyroxene that enclose perovskite (Fig. 3).

Figure 4 shows the Al-Mg isochron diagram of the phases in *3138-F8*, which were previously reported by MacPherson et al. (2012b). Those data were calculated using β = 0.514 for mass dependent fractionation correction. However, the majority of data were obtained from Al rich melilite with low precision EM analyses, so that the choice of β does not modify the isochron slope significantly (Kita et al., 2013). All data, including the ^{16}O-depleted pyroxene that mantles perovskite, are fully isochronous along an isochron corresponding to initial $^{26}Al/^{27}Al = (5.29 \pm 0.28) \times 10^{-5}$ with mean standard weighted deviation (MSWD) = 1.9; $(\delta^{26}Mg)_0 = -0.07 \pm 0.11$ (figure modified from MacPherson et al., 2012b).

NWA 3118 1N-b (henceforth, *1N-b*) is a very large (>1.8 cm), spheroidal CTA inclusion that appears in section as a torus (Fig. 5), the interior “hole” being filled with meteorite matrix. This object actually has the shape of a bowl in three dimensions (Lorenz et al., 2019). *1N-b* is one of the objects in this study that somewhat blur the distinction between CTA CAIs and Type Bs because, although many CTAs contain pyroxene, *1N-b* is unusual in containing abundant large pyroxene crystals (Fig. 6). In all other respects, including textures, *1N-b* is an ordinary CTA. The major constituent is melilite (Åk$_{<1}$ to Åk$_{63}$), along with the pyroxene, spinel, perovskite, and sparse small Fe-Ni metal grains. *1N-b* contains only traces of secondary alteration. Perovskite occurs as two generations: (1) as dense swarms of tiny (1–2 µm) grains that are concentrated in the outermost portions of the CAI, near the WL rim; and (2) as dispersed grains that occur actually within the WL rim sequence, commonly enclosed in spinel. The most aluminous melilite occurs within ~ 200 µm of the rim at the outermost margin of the CAI. The most Mg-rich melilite is always in direct contact with pyroxene (Fig. 6), in a manner that suggests near-eutectic final melt solidification. Like perovskite, pyroxene also occurs as two generations of crystals, in the interior and near the WL rim. The interior pyroxene occurs as equant – in places euhedral – grains up to ~ 1 mm in maximum dimension, although much smaller grains also occur in the interior. The large pyroxene crystals are compositionally zoned in a concentric fashion (Fig. 6), with Ti-Al-rich cores (typically 21 wt.% Al_2O_3, 14 wt.% TiO_2) and more Ti-Al-depleted rims (~17% wt.% Al_2O_3, ≤ 10 wt.% TiO_2). In general, 50–60% of the titanium is trivalent. Small pyroxene crystals are much more Ti-Al-rich (22–27 wt.% Al_2O_3, 18–20 wt.% TiO_2). Pyroxene near the WL rim occurs as irregular and even vermicular masses that generally are in contact with the dense swarms of perovskite. This pyroxene is Ti-rich, especially close to the perovskite. Interior spinel is (as expected) near end-member in composition, with 0.3–0.8 wt. % TiO_2, < 0.1 wt. % CaO, 0.1–0.5 wt. % FeO, and 0.4–0.5 wt. % Cr_2O_3; MnO and SiO_2 are below detection. Spinel near the WL rim is enriched in FeO, > 1 wt. %.

Figure 7 shows the oxygen isotopic compositions of phases in *1N-b*. As was the case for *3138-F8*, the oxygen isotopes in *1N-b* are unusual relative to most CAIs in CV3s. First, melilite is not uniformly depleted in ^{16}O and, as is the case for *3138-F8*, the most ^{16}O-rich melilite is in the outermost portions of the CAI, near the WL rim. Second, the large pyroxene crystals from the interior of the inclusion cover almost the entire isotopic range of ^{16}O in the whole CAI. This is exceptional, and it is systematic as shown in Figure 8. The Ti-rich cores of individual pyroxene crystals are always ^{16}O-depleted (shown in Fig. 8 as small negative Δ^{17}O, which is equivalent to ^{16}O-depletion) whereas the Ti-poor rims are always ^{16}O-rich. Note also on Figure 8 that the ratio of Ti^{3+} to total Ti remains constant throughout the illustrated crystal despite both the isotopic variation and a significant change in total Ti (reported as TiO_2). The correlation between pyroxene isotopic composition and Ti-enrichment holds true in the WL rim as well. Figure 9a is a BSE image of a portion of *1N-b* near the WL rim sequence, showing small pyroxene grains in close association with swarms of tiny perovskite crystals, and also showing a second generation of perovskite crystals enclosed within the WL rim sequence. Figure 9b shows an enlarged BSE image corresponding to the white box of Figure 9a, centered on the WL rim. Figures 9c-e are, respectively, a Mg-Si-Ti element map, a $^{27}Al^{-}/^{16}O^{-}$ SCAPS image, and a $\delta^{18}O$ SCAPS image of that same enlarged region. These images collectively show that the inner Ti-rich pyroxene layer is ^{18}O-rich (= ^{16}O-depleted) whereas the outer diopside layer is ^{18}O-poor (^{16}O-rich). Of importance later, note also in Figure 9 that perovskite also is ^{18}O-rich (^{16}O-depleted).

Figure 10 shows the Al-Mg isotopic systematics of *1N-b*. All phases conform closely to a single isochron, yielding initial $^{26}Al/^{27}Al = (4.81 \pm 0.11) \times 10^{-5}$ and MSWD = 0.73; $(\delta^{26}Mg)_0 = 0.06 \pm 0.03$. The pyroxene data plotted in Figure 10 include grains that are Ti-rich and ^{16}O-depleted as well as grains that are relatively Ti-poorer and ^{16}O-richer; in terms of Al-Mg isotopic systematics, there is no difference between the two except in $^{27}Al/^{24}Mg$ ratios.

NWA 3118 16N (henceforth, *16N*) is an oblong CTA inclusion, only a portion of which is contained within the thin section (Fig. 11). The maximum dimension in the section is ~ 0.8 cm, so the original CAI undoubtedly exceeded 1 cm in size. Like *1N-b*, *16N* is unusual for a CTA CAI because it contains not only abundant pyroxene but also small amounts of primary anorthite; it is transitional to a Type B. The most abundant phase, melilite, has a composition range $Åk_{2-58}$ with an average composition of $Åk_{24}$. As in *1N-b*, the most aluminous melilite is located in the outermost margin of the CAI near the WL rim, and the most magnesium-rich melilite is in contact with interior pyroxene and anorthite (Fig. 12a-b), consistent with the eutectic assemblage for an igneous melt of this bulk composition. Like *1N-b*, *16N* contains abundant large pyroxene crystals but, as just noted, also contains dispersed, small, irregularly shaped grains of anorthite. Spinel, perovskite, and numerous small Fe-Ni metal beads are accessory phases. Trace amounts of sodium-rich secondary alteration occur locally in patches. Perovskite is most abundant in the outer margins of the CAI and occurs as swarms of irregular crystals that locally are as large 50 μm in maximum dimension. The pyroxene occurs as grains up to ~0.5 mm in maximum dimension, ranging in size down to less than 10 μm. Unlike the pyroxene in *1N-b*, all but the very largest pyroxene crystals in *16N* are irregular in shape and in places take the form of stringers or spongy (poikilitic) crystals (Fig. 12c-d). Pyroxene in the outermost part of the CAI is second generation, as in *1N-b*. These crystals are small, very Ti-rich, and always occur near or in contact with perovskite. Their TiO_2 content decreases with increased distance from the perovskite. The large interior pyroxene crystals have a wide range in composition, 17.7–22.7 wt.% Al_2O_3, 7.4–14.4 wt.% TiO_2, and are compositionally zoned with Ti-Al-rich cores and Ti-Al-poorer rims. On average about 74% of the titanium is trivalent. Interior spinel is near-end-member $MgAl_2O_4$, with up to 0.65 wt.% TiO_2

and 0.37 wt.% FeO, and 0.1 wt.% Cr_2O_3; other minor elements are at or near detection limits. Spinel in the WL rim contains up to (at least) 2.6 wt.% FeO and 0.4 wt.% Cr_2O_3; MnO and SiO_2 are below detection. Anorthite is close to end-member in composition; elevated Na_2O in a few locations hints at minor secondary alteration. Despite the irregular shapes of the anorthite regions, cathodoluminescence imaging reveals that the irregular anorthite regions consist of large single crystals (Fig. 13). This feature is consistent with such anorthite being igneous in origin, as noted above.

Figure 14 shows the oxygen isotopic composition of phases in *16N*. Melilite is nearly uniformly depleted in ^{16}O ($\Delta^{17}O$ range from ~ −5 to ~ −2‰), and spinel is uniformly enriched. Anorthite is variably depleted in ^{16}O ($\Delta^{17}O$ ~ −14 to ~ −5‰). Perovskite is one of the most ^{16}O depleted phases in *16N* ($\Delta^{17}O$ ~ −2‰). Similar to *1N-b*, the pyroxene in *16N* shows a wide range in oxygen isotopic composition from ^{16}O-rich to ^{16}O-poor ($\Delta^{17}O$ ~ −22 to ~ −3‰). And again, like in *1N-b*, ^{16}O-depletion is correlated with Ti-enrichment (Fig. 15). The most ^{16}O-rich pyroxene is diopside in the WL rim sequence (Fig. 14) and the Ti-depleted portions of the large interior pyroxene crystals. The oxygen isotopic and spatial relationship between pyroxene and perovskite is especially enlightening, as shown in Figure 16. As noted above, perovskite is concentrated in the outer margin of the CAI. Pyroxene in this same region occurs as small anastomosing ("spongy") grains associated closely with the perovskite. Pyroxene closest to or contacting the perovskite is very Ti-rich, and the Ti content decreases with increasing distance away from the perovskite. As will be discussed below, this observation suggests a genetic relationship between the two phases in which the pyroxene is forming at the expense of the perovskite. In this context, the crucial point is that the perovskite is ^{16}O-poor, and all of the pyroxene in its immediate vicinity is likewise ^{16}O-poor (Fig. 16; note that the spots marked on Fig. 16 were not analyzed by electron microprobe and so the isotopic compositions are not shown on Fig. 15).

Figure 17 shows the Al-Mg isotopic systematics in *16N*. Except for anorthite (not used in the regression), most of the data adhere closely to a single isochron with some scatter, initial $^{26}Al/^{27}Al = (5.15 \pm 0.10) \times 10^{-5}$, and MSWD = 3.9; $(\delta^{26}Mg)_0 = -0.04 \pm 0.03$. Most anorthite analyses scatter widely to the right (high $^{27}Al/^{24}Mg$) side of the isochron, suggesting secondary exchange of magnesium with a low Al/Mg phase such as spinel (*e.g.,* MacPherson et al., 2012b). Like *1N-b*, there is no difference between the Ti-rich (^{16}O-depleted) pyroxene and the Ti-poor (^{16}O-rich) pyroxene other than $^{27}Al/^{24}Mg$.

Vigarano 1623-11 (Fig. 18; hereafter, *1623-11*) is an oblong compact Type A, roughly 3×2 mm in size, that consists mainly of melilite, spinel, Ti-rich pyroxene, primary anorthite, trace Fe Ni metal, and minor perovskite that is confined to the rim of the inclusion. A nearly continuous WL rim sequence envelopes the CAI and consists mainly of spinel and aluminous diopside plus forsterite and (locally) fine-grained perovskite. Unlike many Vigarano CAIs, *1623-11* contains significant alteration in the form of fine-grained secondary anorthite and sodium-rich feldspathoids. This alteration is most prominent near the outer margins of the CAI, just beneath the WL rim sequence.

The outermost 50−200 μm region of *1623-11* is relatively simple, being composed mainly of melilite that is relatively unzoned and in the composition range Åk$_{19}$ to Åk$_{39}$. In the interior of the inclusion, melilite is much more variable. In densely crystalline melilite regions away from pyroxene and anorthite, melilite crystals have Al-rich cores (mostly Åk$_{15}$ to Åk$_{25}$) enclosed by thin magnesium-rich rims (mostly Åk$_{40}$ to Åk$_{60}$). Melilite near regions of anorthite and pyroxene (Fig. 19a-b) is strongly zoned, and the most magnesium-rich melilite (up to Åk$_{73}$) is in contact with pyroxene and anorthite, similar to *1N-b* and *16N* and again consistent with the eutectic assemblage for an igneous melt of this bulk composition. Closer examination of the melilite grains that are enclosed by anorthite (Fig. 19c-d) shows that they are rounded tabular crystals that largely are unzoned and aluminous, mostly Åk$_{15}$ to Åk$_{25}$. The anastomosing plagioclase regions themselves are nearly pure anorthite and, as shown by cathodoluminescence imaging (Fig. 20), are relatively coarse-grained single crystals. Pyroxene in the WL rim of *1623-11* is Ti-poor, mostly < 1 wt.% TiO_2 (calculating all Ti as Ti^{4+}); pyroxene in the interior of the CAI is strongly zoned from Ti-rich crystal centers to Ti-poor rims, mostly in the range 4−15 wt. % TiO_2 and about ½ of which is trivalent. Interior spinel is exceptionally pure $MgAl_2O_4$, and even in the WL rim contains < 2 wt.% FeO.

Oxygen isotopes were not measured in *1623-11*. The Al-Mg systematics of *1623-11* are shown in Figure 21. All phases adhere closely to a single isochron, corresponding to initial $^{26}Al/^{27}Al = (4.94 \pm 0.07) \times 10^{-5}$, and MSWD = 2.8; $(\delta^{26}Mg)_0 = -0.03 \pm 0.02$.

Allende TS19-F1 (henceforth, *TS19-F1*) is a 3.2 × 1.6 mm oblong CTA inclusion (Fig. 22) that was described in detail by Simon et al. (1999). Melilite mostly is in the composition range Åk$_{13-56}$ (Simon et al., 1999), although those authors also noted the presence of nearly pure gehlenite (<Åk$_1$) at the extreme margin of the inclusion. The melilite in *TS19-F1* is normally zoned, consistent with solidification from a melt (Simon et al., 1999). A number of the melilite laths are oriented at high angles to the margin of the CAI, suggestive of melt crystallization from the outside inwards (e.g., MacPherson and Grossman, 1981). Accessory minerals are perovskite and spinel. The perovskite crystals are most notable for their very rounded shapes (Fig. 23), indicating that they were not in equilibrium with the rest of the CAI at the time of solidification. Trace amounts of titanium-rich pyroxene occur only as very thin rims around perovskite (Fig. 24a b) and as small inclusions within perovskite and spinel (Figs. 24c-d). A minor amount of pyroxene also occurs in the WL rim sequence. Surprisingly for an Allende CAI, *TS19-F1* contains only trace amounts of sodium-rich alteration, mainly in the WL rim. The interior melilite is essentially unaltered.

The oxygen isotopic compositions of phases in *TS19-F1* are shown in Figure 25. Melilite is uniformly depleted in ^{16}O, and spinel is uniformly ^{16}O-rich. Perovskite is variably enriched in ^{16}O, and never as ^{16}O-depleted as perovskite in *3138-F8* or *16N*. Pyroxene rims on perovskite are ^{16}O-depleted, whereas pyroxene inclusions within spinel and perovskite are ^{16}O-rich.

The Al-Mg isotopic systematics are shown in Figure 26. Melilite and spinel define an isochron with initial ^{26}Al/^{27}Al = (4.89 ± 0.12) × 10^{-5}, $\delta^{26}\mathrm{Mg}_0$ = 0.17±0.04, and MSWD = 2.3. We were unaware of the tiny pyroxene grains at the time the Al-Mg isotopic analyses were made, so they were not measured.

Summary Observations

We studied five Type A CAIs, one FTA and four CTAs. The Fluffy Type A (*3138-F8*) shows no indication of any melting. All the Compact Type As show clear indications of partial melting.

The five CAIs show a small spread of initial ^{26}Al/^{27}Al ratios, (4.81−5.29) × 10^{-5} (Fig. 27), corresponding to a maximum difference in formation ages of about 96,000 years if we assume nebular homogeneity in ^{26}Al at the canonical level of ^{26}Al/^{27}Al = (5.23 ± 0.13) × 10^{-5} (Jacobsen *et al.*, 2008).

In two of the CAIs where we were able to measure its oxygen isotopic composition, perovskite is the most (or nearly so) ^{16}O-depleted phase in those CAIs. In *TS19-F1* however, perovskite is variably ^{16}O-enriched. Pyroxene that mantles or is near perovskite is ^{16}O-depleted, including *TS19-F1*, but pyroxene inclusions within perovskite in *TS19-F1* are ^{16}O-rich.

The inclusion *1N-b* contains two clear generations of pyroxene: primary igneous pyroxene in the CAI interior shows inverse oxygen isotopic zonation (i.e. the Ti-rich cores are ^{16}O-poor), and a very fine-grained second generation that is forming at the expense of perovskite near the outer margins of the CAI. In this secondary pyroxene, that closest to the perovskite is very Ti-rich and ^{16}O-poor and with increasing distance from the perovskite becomes less Ti-rich and more ^{16}O rich. Pyroxene in inclusion *TS19-F1* occurs as rims on perovskite and as inclusions within both perovskite and spinel, and these also may represent two generations of pyroxene.

DISCUSSION

Differing histories of the five CAIs

The differing petrographic textures of Types A and B inclusions are reflective of their differing histories, and essential to this work. Type B inclusions are characterized by lathlike melilite and anorthite crystals, both commonly subhedral in shape, separated by intergranular to sub-ophitic pyroxene crystals; spinel grains are enclosed by all other phases, demonstrating that it was the first crystallizing (liquidus) phase. Type B melilites are characterized by "normal" igneous zoning, with relatively aluminum-rich cores that zone gradually outwards to magnesium-rich exteriors. This zoning is in accord with the experimentally-determined binary melt system gehlenite-åkermanite. Type B pyroxenes are always more titanium- and aluminum-rich in their interiors and less so in their exteriors. All these features are consistent with the inclusions having been largely – but not completely – melted, (Stolper and Paque, 1986). Some CTAs show similar features (Simon et al., 1999) but most CTAs and all FTAs are very different. Melilite generally occurs as approximately equant crystals in a dense polygonal-granular texture; zoning is slight and, especially in Fluffy Type As, is "reversed" with aluminous rims over more magnesium-rich interiors (MacPherson and Grossman, 1984). This feature cannot be explained by simple igneous crystallization. As shown earlier in this paper, pyroxene can have a variety of textures, from relatively large and well-formed crystals (as in *1N-b*) to spongy anastomosing grains near or mantling perovskite crystals. Anorthite is rare in CTAs but, where present as in *16N* and *1623-11*, is not tabular or subhedral. It occurs as spongy crystals in association with pyroxene and Mg-rich melilite. All of these features indicate that most CTAs were only slightly melted, above the temperature of the quaternary eutectic (see below) but not by much.

Vigarano *3138-F8* and *1623-11*, Allende *TS19-F1*, and NWA *1N-b* and *16N* all are Type A inclusions, consisting mainly of melilite. However, the five experienced different histories. The most gehlenite-rich object is *3138-F8*, which is a FTA: an aggregate object that never experienced melting. At most it experienced sintering. Abundant hibonite in its core, enclosed in melilite, is consistent with the relative condensation sequence of the two phases and indicates that this object preserves some primary condensation features. *1623-11*, *TS19-F1, 1N-b,* and *16N* are Compact Type As: they all experienced minor partial melting, perhaps to a somewhat greater degree in *TS19-F1* and *1Nb* than in the others (see below). Only in *TS19-F1* does some melilite occur as continuously and normally-zoned lath-shaped crystals like the ones in Type Bs (Simon et al., 1999), but even in *TS19-F1* the composition range is nowhere near as great as in Type Bs.

The bulk compositions of the five inclusions are plotted in Figure 28 on the phase diagram anorthite-forsterite-gehlenite, as projected from spinel (Stolper, 1982). Shown for reference are the approximate composition fields for Type A and Type B CAIs (based on data from Beckett, 1986; Simon and Grossman, 2004; and Ivanova et al., 2021). On this diagram, the quaternary eutectic (melilite + calcic pyroxene + anorthite + spinel) is the point where the fields of melilite, anorthite, and pyroxene meet; the melt temperature at the eutectic is approximately 1230 °C (Stolper, 1982). In melts of Types A and B CAI composition, which lie largely within this system, the crystallizing melilite always becomes more Mg-rich with falling temperature. At the quaternary eutectic, the final melilite composition in *e.g.*, Type B CAIs usually approaches ~Åk$_{71}$ (Beckett, 1986), the composition of the minimum in the gehlenite-åkermanite binary system. Most Compact Type As (*e.g., 1N-b)* lack anorthite (Simon et al., 1999) and thus their melts never reached the quaternary eutectic; their final melilite composition is less Mg-rich than the melilite binary minimum. Allende *TS19F1, 1N-b,* and *16N* all plot in the Type A compositional field, whereas *1623-11* plots in the Type B field owing to its significant anorthite content. In *1623-11*, *1N-b,* and *16N*, the close association of the most Mg-rich melilite being always in contact with pyroxene and (in the case of *1623-11* and *16N*), anorthite, is strongly suggestive of a eutectic melt assemblage (unrelated to the fact that the phases are not in oxygen isotopic equilibrium, which is the result of later subsolidus exchange and has nothing to do with igneous crystallization). *TS19-F1* contains neither igneous pyroxene nor anorthite, but has normally-zoned melilite crystals that are consistent with melt solidification (Simon et al., 1999). Thus, the melt composition in this object never even reached the melilite + anorthite (+ spinel) cotectic. *1623-11* and *16N* do contain both pyroxene and anorthite. The most magnesium-rich melilite in *1623-11* is Åk$_{72}$ and the melt composition was clearly that of the quaternary eutectic, whereas the most magnesium-rich melilite in *16N* is nowhere near Åk$_{72}$.

The critical difference between the melt textures in these Compact Type As and those in Type B CAIs is that these are primarily partial melting textures, rather than reflecting near complete liquid line-of-descent melt crystallization of mostly molten objects. In *1623-11* for example, the anorthite takes the form of very irregular spongy crystals that poikilitically enclose small tabular melilite crystals (Fig. 19). In Type Bs, anorthite always occurs as lathlike subhedral crystals. In terms of mineralogy and bulk composition, *1623-11* is a Type B, but texturally it is a Compact Type A. In *16N*, the pyroxene also occurs as poikilitic spongy crystals enclosing small melilite tablets (Fig. 12). In Type Bs, pyroxene encloses only spinel crystals and at most shows a subophitic relationship with melilite and anorthite. Texturally *16N* is a Compact Type A but, although it has less anorthite than does *1623-11*, had *16N* been fully melted and then solidified, it likely would be called a Type B. The melilite in all of these Compact Type As occurs mostly as dense polygonal-granular intergrowths, with the individual crystals showing very little in the way of compositional zoning. Melilite in Type Bs always occurs as subhedral lath-like crystals with very strong compositional zoning, having gehlenitic cores overlain by progressively more magnesium-rich mantles. *1N-b* and *TS19-F1* arguably experienced a greater degree of partial melting than did the other Compact Type As in this study, judging from of the coarse-grained and locally euhedral nature of pyroxenes in *1N-b* (e.g., Figs. 6, 8) and the normally zoned melilites in *TS19-F1*. Yet, the melilite in *1N-b* is similar to that in *1623-11* and *16N*.

Formation of Ti-rich pyroxene: Perovskite is the key

Understanding the perovskite

The textures in *3138-F8*, *1N-b*, *1623-11*, *TS19-F1* and *16N* inextricably link the formation of Ti-rich pyroxene to a reaction involving perovskite and melilite (Figs. 2, 9, 16, 24). In a general way, the oxygen isotopic compositions (other than in *TS19-F1*; discussed below) and mineral chemistry support this genetic relationship. In order to begin this discussion, it is necessary to understand where the perovskite itself comes from. Complicating matters, there are three generations of perovskite represented in the CAIs on this study: fine-grained swarms of small crystals that occur near the WL rims sequences (such as in *1N-b* and *16N*), larger isolated crystals in CAI interiors (e.g., *TS19-F1*, *3138-F8*), and in one case perovskite within the WL rim sequence itself (e.g., *1N-b*).

In un-melted inclusions, such as FTA CAIs like *3138-F8*, perovskite occurs as isolated grains enclosed within primary phases such as melilite or, in silicate-poor aggregate CAIs such as the spinel-rich inclusions found in many kinds of carbonaceous chondrites – spinel and hibonite (recent examples shown in MacPherson et al. 2020, their Figs. 7, 11, and 24; also, in older references such as MacPherson *et al*., 1983, 1984; Ireland, 1988; MacPherson and Davis, 1994). Because the CAIs themselves are un-melted, the perovskite did not crystallize from a melt. During equilibrium condensation of a hot solar gas, perovskite is predicted to condense prior to (at higher temperature than) melilite and somewhat after hibonite. Thus, in all un-melted CAIs, perovskite is reasonably assumed to be a primary nebular condensate that became trapped within later condensing phases. This likely is true also for perovskite within the interiors of melted (i.e. Compact) Type As, but the reasoning is more complicated. The question is whether such perovskite could instead be the product of melt solidification, and the likely answer is no. For perovskite to be an igneous phase in a silicate melt, it would have to precipitate prior to any pyroxene whose crystallization would pre-empt the formation of perovskite at all (see Simon et al., 1999, for a dissenting view; but they claim that perovskite crystalized late in the CAIs they studied, which most of their own photomicrographs do not support). Few CAIs have more than ~3 wt.% TiO_2 in bulk.

Beckett and Stolper (1991) conducted experiments on CAI-like silicate melts with up to 5 wt.% TiO_2 and did not report perovskite among any of the run products. From a textural point of view, we are unaware of any Type A or Type B CAI in which perovskite is an unambiguous igneous phase. In summary, in all igneous silicate-rich CAIs, we consider interior perovskite to be a relict phase that survived melting.

However, the very fine-grained perovskite found near the margins of many CTA CAIs (e.g., *1N-b*) is different. It may have solidified from a later melt that experienced significant melt evaporation from the outermost surface. This evaporation would have led to major enrichment in TiO_2 in the residual melt, sufficient to stabilize perovskite as a crystallizing phase. This is exactly how we interpret the fine-grained perovskite in *1N-b* and *16N*.

Formation of the pyroxene from perovskite

Considering the actual compositions of the Ti-rich pyroxene and its enclosing melilite in the studied CAIs, a reaction can be written that does not require the addition of any external components:

$$Ca_2Mg_{0.2}Al_{1.6}Si_{1.2}O_7\ (\text{Åk}_{20}) + 0.5CaTiO_3 + 0.15H_2 \longrightarrow \quad (3)$$

$$CaMg_{0.2}Ti^{3+}_{0.3}Ti^{4+}_{0.2}Al_{1.3}SiO_6 + 1.5\ CaO + 0.15Al_2O_3 + 0.2SiO_2 + 0.15H_2O$$

The resulting pyroxene contains 50% diopside, 10% $CaTi^{3+}AlSiO_6$, 10% $CaTi^{4+}Al_2O_6$, and 30% Ca-Tschermak's molecule (kushiroite), which is very close to the average composition of the most Ti-rich pyroxenes in the studied CAIs (Table 3).

If the formation of pyroxene from perovskite, and the transition from Type A to Type B, is essentially isochemical (other than SiO_2; see below) as we propose, it is reasonable to ask whether there is sufficient perovskite in Type As to actually account for the abundant Ti-rich pyroxene observed in Type Bs. Figure 29 is a histogram of TiO_2 abundances in Type A and Type B CAIs. The two varieties of CAI largely overlap in their TiO_2 contents, indicating that the observed abundance of perovskite in Type As is in fact sufficient to form the abundant Ti-rich pyroxene in Type B CAIs.
The reaction (3) as written does not exactly balance between only the stoichiometric reactants (melilite + perovskite) and products (pyroxene), although slight changes in the reacting melilite composition could probably eliminate the excess Al_2O_3 from the products. The excess silica, if real, could contribute slightly (not significantly) to the formation of anorthite (see below). The main point is that no additional external components are required. The question then becomes, why such a

reaction took place at all? One possibility is that it was triggered by a change in redox conditions. If so, the implication is that the perovskite originally formed under less reducing conditions than those required to stabilize pyroxene. The only quantitative estimate for the fO_2 under which CAIs formed comes from the experimental work of J. Beckett (Beckett, 1986; see Grossman et al., 2008). But that work was aimed at determining the nebular conditions under which the pyroxene in igneous Type B CAIs formed. *It said nothing directly about the prior nebular conditions under which perovskite condensed.*

Formation of anorthite: The critical role of silica addition in the formation of Type B CAIs

Unlike pyroxene, the formation of anorthite in a Type A inclusion requires the addition of silica. The reaction relating melilite-rich Type A CAIs to anorthite-bearing Type Bs can be written simply:

$$Ca_2Al_2SiO_7 + 3SiO + Mg + 4H_2O \rightarrow CaAl_2Si_2O_8 + CaMgSi_2O_6 + 4H_2 \quad (4)$$

In equilibrium condensation calculations such as those of Yoneda and Grossman (1995), anorthite does not form by reaction of melilite with the gas. Rather, it condenses independently after condensation of forsterite. Yet the existence of anorthite-bearing Type B CAIs that do not contain forsterite suggests that anorthite formed by another mechanism and prior to forsterite. The existence of anorthite-rich domains in forsterite-free fine-grained CAIs (Krot *et al.*, 2004) also supports this idea. One suggestion (MacPherson et al., 2004; Petaev and Wood, 1998; 2005; Krot et al., 2007) is based on the fact that the relative equilibrium condensation temperatures of anorthite and forsterite are pressure dependent, with anorthite condensing prior to (at higher temperature than) forsterite as $P_T < 10^{-4}$ bars, lower than the usual pressure of 10^{-3} bars that is assumed in most condensation calculations (including Yoneda and Grossman, 1995).

The evidence in two of the inclusions studied herein suggests a different mechanism, namely the addition of silica prior to or during melting. The CAIs *16N* and *1623-11* both contain numerous very irregular patches of anorthite (Figs.12, 13, 19, 20) that, upon examination using cathodoluminescence, prove to be poikilitic single crystals. We interpret these anorthite grains to be igneous in origin. They can only have formed if silica was added to the inclusion from the gas, prior to or during melting. In that case, the only real distinction between these two CTAs and Type B CAIs is the degree of melting (see above). More extensive melting would have caused the anorthite ultimately to have crystallized as coarse and relatively euhedral crystals. The silica need not have been added during melting. A common feature in Fluffy Type As is the occurrence of anorthite as secondary veins cross cutting the inclusion, and apparently replacing melilite. Figure 30 is an image of one such occurrence in a different FTA, Vigarano *477-5*, in which the anorthite clearly is rimming the melilite. Melting of such an assemblage certainly would result in the kind of spongy anastomosing anorthite crystals such as those seen in *16N* and *1623-11* and noted above.

Lin and Kimura (2003) suggested an alternative model for the formation of Type Bs, based solely on bulk compositional overlap between the Type A CAIs they studied in Ningqiang Type and the Type B CAIs found in typical CV3 chondrites. Their model did not involve addition of silica (or reaction of perovskite), but did involve melting of Type A precursors. However, their measured bulk compositions specifically included the Wark-Lovering rim sequences, which contain abundant diopside. Melting of the CAI interior compositions, minus the rims, would not result in the formation of Type B CAIs unless silica is introduced. Evidence for melting of pre existing WL rim sequences in any CAIs is very rare (*e.g.* Wark and Lovering, 1980), and that interpretation is open to debate.

Evolution of fO_2 and ^{16}O in the nebular oxygen reservoir

The approximately slope-1 array of oxygen isotopic compositions of CAI minerals along CCAM generally is interpreted as sub-solidus exchange of originally ^{16}O-rich minerals with a ^{16}O depleted external reservoir (Clayton et al., 1977). In the latter model, the exchanging reservoir was the nebular gas. Others have argued (*e.g.* Bodenan *et al.,* 2014; Krot *et al.*, 2021) that the exchange reservoir was fluid on the CV parent body. As discussed below in the section "*An unresolved problem regarding perovskite, pyroxene, and oxygen isotopes",* we concede that this is a possible model that can only be tested by experimental determination of oxygen diffusion coefficient in pyroxenes of differing composition. Pending such experiments, we argue here that the reservoir was probably nebular rather than parent body.

The isotopic compositions of the large igneous pyroxenes in *1N-b* and *16N* are clearly correlated with pyroxene chemical composition. The Ti-rich crystal interiors and Ti-poor crystal rims are a normal crystal growth pattern for igneous pyroxenes such as those in Type B CAIs (e.g., Simon et al., 1991). The isotopic compositions of these single crystals span nearly the entire range of CCAM up to the terrestrial fractionation line ("TF" on the figures), as the crystal rims are ^{16}O rich, these crystals evolved isotopically *down* the CCAM line during crystal growth rather than up. There are two possible explanations for this observation. One is that both the pyroxene and perovskite formed with ^{16}O-rich compositions and that both experienced secondary isotopic exchange with a ^{16}O-poor reservoir. Pyroxene is generally assumed to be resistant to any kind of isotopic resetting, but this exchange model implies that Ti-rich pyroxene in fact is much more susceptible to exchange than more diopsidic compositions. This needs to be tested experimentally. The second model, explored here, is that the ^{16}O-poor crystal interiors and the ^{16}O-rich crystal rims are a crystal growth phenomenon and have nothing to do with late-stage exchange *via* solid state diffusion.

Following our initial observation of this phenomenon (MacPherson et al., 2012a), Kawasaki et al. (2018) observed a similar distribution of oxygen isotopes in pyroxene from a Type B CAI from Allende. They interpreted this as due to an evolving oxygen isotopic reservoir while the molten object was cooling and crystallizing. The obvious problem with their model is that the reservoir would have had to evolve during the very short time span of melt solidification (~ 1 day at 10°C/hour cooling rate; MacPherson et al., 1984; Stolper and Paque, 1986; (~ 5-10 days at 0.1-0.5°C/hour; Yamamoto *et al.,* 2021).

Aléon (2018) proposed yet a different model to explains some similar observations in another Type B CAI, in which an ^{16}O-rich solidifying melt exchanged oxygen isotopes with an external gaseous reservoir during crystallization, but mostly following the crystallization of spinel. Subsequent closed-system reheating resulted in redistribution of the isotopes internally such that only spinel retained its original ^{16}O-rich composition. A serious problem with this model is the failure to recognize that spinel does not cease to crystallize once melilite begins. It continues to crystallize all the way down to the solidus. This later-crystallizing spinel should be ^{16}O-depleted. Thus Aléon’s model cannot explain the uniform ^{16}O enrichment in Type B spinel. Also, Aléon's model was based on textures that seemed to indicate a reaction relationship between pyroxene and spinel. Textural interpretations are always somewhat subjective, and in our opinions many of the textures he showed were simply pyroxene poikilitically enclosing spinel grains. It *is* common for spinel in the exterior portions of many Type B CAIs to show dissolution textures, but these are due to surface evaporation of magnesium from the melt. Such evaporation leads to destabilization of spinel and its dissolution, but pyroxene is not involved. There is no basis in phase equilibria for spinel, in a closed system, to react with the melt to form pyroxene. Aléon's model also cannot explain why only the most Ti-rich pyroxenes are ^{16}O-depleted, and in many CAIs with pyroxenes that are only moderately Ti-rich, the pyroxenes are ^{16}O-rich.

Our observations point to a very different model. The key is the observed ^{16}O-poor isotopic compositions of the perovskites in our Type A CAIs, and the observation that ^{16}O-poor pyroxene commonly encloses perovskite. The pyroxene initially formed by reaction of perovskite with melilite, and although the perovskite was ^{16}O-poor the melilite was ^{16}O-rich at the time of the reaction. The reaction between the perovskite and the melilite, via reaction #3, must have occurred after perovskite exchanged its oxygen isotopes but *prior to melilite doing so*. Thus, the pyroxene crystals initially formed with a ^{16}O-depleted composition inherited from the perovskite, then became progressively more ^{16}O-rich as the then ^{16}O-rich melilite isotopic reservoir began to dominate. Only subsequent to this process did the melilite itself exchange. Although literature values vary widely (Robens et al., 2021), oxygen apparently diffuses in perovskite more rapidly than even in melilite. A comparison of the data for åkermanite, anorthite, pyroxene, and spinel (all from Ryerson and McKeegan, 1994) with data for perovskite from Sakaguchi and Haneda (1996) shows that at 1400°C oxygen diffusion in perovskite is ~10^{2}× faster than in åkermanite and ~10^{6} × faster than in spinel. At 1000°C, oxygen diffusion in perovskite is still 10× faster than in åkermanite. These are conservative estimates: according to Robens et al. (2021), the experimentally-determined values are orders of magnitude too slow and incorrect.

This model also may resolve a long-standing debate about the origin of the internal oxygen isotopic mixing line that characterizes CV3 CAIs. The classic model of Clayton et al. (1977) is that uniformly ^{16}O-rich CAIs experienced later diffusion-controlled sub-solidus exchange with a ^{16}O-poor gas, the idea being that rapidly-diffusing minerals (anorthite and melilite) exchanged readily with the external reservoir whereas the slow-diffusing minerals (pyroxene and spinel) exchanged little if at all. But Ryerson and McKeegan (1994) experimentally determined the diffusion coefficients of the primary CAI minerals and concluded that the Clayton et al. model did not work because diffusion coefficients for pyroxene were much slower than those for spinel and anorthite. Thus, pyroxene should (in the Clayton model) be ^{16}O-rich relative to spinel and anorthite, but in the case of spinel this is the reverse of what is observed. Thus, Ryerson and McKeegan concluded that "processes other than diffusion and partial melting must play a predominant role in controlling O-isotope compositions of CAI minerals". Specifically, they advocated a model in which originally ^{16}O-rich CAIs were later remelted within an ^{16}O-poor gas, then slowly equilibrated with that gas during progressive igneous crystallization. The relative enrichment/depletion in ^{16}O of each crystallizing phase was a function of its order of appearance in the igneous crystallization sequence. Yet the Ryerson and McKeegan model is problematic too: in some Type B CAIs the anorthite is equally ^{16}O-rich to the pyroxene, and both are ^{16}O-rich relative to the melilite that precedes them during igneous crystallization of a Type B melt. Our results suggest that the original formation of pyroxene from ^{16}O-poor perovskite is responsible both for the apparent spinel-pyroxene discrepancy pointed out by Ryerson and McKeegan and also the ^{16}

O-poor composition of the pyroxene cores in the Type B CAI studied by Kawasaki et al. (2018). Because even in Type Bs the melting is never total, the initial ^{16}O-poor isotopic composition of the pyroxene is rarely erased in its entirety.

The ^{16}O-depleted pyroxene in *3138-F8*, *1N-b*, and *16N* is isochronous within error of the other phases (including the ^{16}O-rich pyroxene) in each inclusion. The Ti^{3+}/Ti^{4+} ratios of the pyroxene remain constant (on average ~60% Ti^{3+}) independent of the oxygen isotopic compositions (e.g., Fig. 8) Together, these observations show that, once the pyroxene formed, oxidation state and oxygen isotopes were decoupled during CAI formation, and that this decoupling lasted for at least 96,000 years, based on the difference in initial ^{26}Al/^{27}Al ratios between *3138-F8* and *1N-b*. In the context of our model, a corollary is that extreme oxygen isotopic variations in CAIs were established very early and, again, were independent of fO_2. In particular, perovskite either formed in or exchanged with a ^{16}O-poor nebular reservoir prior to the formation of the ^{16}O-rich minerals that generally characterize CAIs. It is unknown what or where that ^{16}O poor and low fO_2 reservoir was. J. Simon et al. (2011) argued that transport of CAIs across differing reservoirs was responsible for isotopic variations across WL rim sequences, but they also observed apparent observed changes in fO_2. But S. Simon et al. (2012) disputed the fO_2 variations, and in any case the primary (interior) pyroxenes in our Type A CAIs show no such changes in inferred valence state regardless of level of ^{16}O enrichment or depletion.

Reconciling with evidence from mass-dependent isotopic fractionation

Abundant evidence exists to show that Type B CAIs underwent surface melt evaporation (see e.g., Grossman et al., 2000; Richter et al., 2007; Grossman et al., 2008; Bullock et al., 2013), in the form of loss of magnesium and enrichment of the heavy isotopes of magnesium and silicon (see review and discussion by Richter et al., 2007). This would seem to be in contradiction to our model in which addition of silica is required for the formation of anorthite. In fact, there is no contradiction because both addition and evaporation occurred – just not simultaneously. The fact is that overall there must have been a net addition of silica in order to transform a Type A into a Type B. Melt evaporation was a surface process occurring along the outermost margin of the molten CAIs, whereas addition of silica occurred while the inclusion was solid, via reaction of the melilite with gas from the external nebula that permeated the CAIs along fractures and grain boundaries as we have shown herein (e.g. Fig. 30). Overall, the addition of silica was the more dominant process.

Evolution of the reservoir

Clearly the CAIs studied here, by Kawasaki et al. (2018) and by Aléon (2018) were exposed to multiple isotopic reservoirs during their complex formation. Either the CAIs moved between ^{16}O-rich and ^{16}O-poor reservoirs, or the oxygen isotopic composition of the reservoirs themselves changed drastically during CAI evolution. The Kawasaki et al. (2018) model requires either alternative to be extraordinarily rapid (~ one to a few days; see also Yamamoto *et al.,* 2021). We propose a very different model, one in which the reservoir evolves between ^{16}O-rich and ^{16}O poor over a period of weeks to months. The cause is FU-Orionis type flare-ups in the infant proto Sun that expand and contract the ^{16}O-rich "bubble" in the inner solar system (< ~1 AU from the Sun) surrounding the proto-Sun. The process is illustrated schematically in Figure 31.

The diagram is based on the conventional oxygen 3-isotope plot, showing the terrestrial fractionation line (T) and the Carbonaceous Chondrite Anhydrous Mineral line (CCAM; Clayton et al., 1977), which is slightly shallower in slope that the Primitive Chondrule Mineral line (PCM; Ushikubo et al., 2012). The isotopic composition of the Sun is taken to be δ^{18}O = −58.5‰, δ^{17}O = −59.1‰ (McKeegan et al., 2011). We assume that CCAM and PCM are mixing lines between the ^{16}O-rich composition of the Sun and ^{16}O-depleted outer solar system ices (δ^{17}O, δ^{18}O ~ +180‰; Sakamoto et al., 2007). Large star-shaped yellow symbols represent the ambient CAI reservoir when the proto-Sun in a flare-up phase, and small symbols represent a quiescent phase.

FU Orionis flares are believed to be caused by non-linear accretion of matter from the accretion disks onto growing proto-stars, and result in rapid increases in observed brightness of several magnitudes (e.g., Audard et al., 2014) followed by a much more gradual decline. The time interval between such outbursts has never been directly observed, but is estimated to be on the order of $10^4$to 10^5 years. Such outbursts are thought to be common in all solar-mass young proto stars. Boss et al. (2012) modeled the thermal consequences of such an outburst in our young proto Sun and estimated that temperatures could have reached 1500K at 1 astronomical unit (AU) distance from the Sun. Our model assumes that one or several such outbursts did occur in the proto-Sun. Figures 31a−c represent the first major flare-up during which inner solar system matter was mostly to completely evaporated, followed by condensation of the first generation CAIs (for the sake of this discussion, we ignore a possible earlier episode that caused formation of FUN CAIs and their relatives, prior to introduction of ^{26}Al). At the stage represented by Figure 31b the inner solar system out to approximately 1 AU (at 1500 K, this is the approximate location of the "rock line"), including all CAIs, was largely ^{16}O-rich. Subsequent to the decline of the flare-up, outer solar system ice (and other solids) gradually drifts inward; mixing of inner solar system gas with evaporated ice leads to a gas composition at ~ 1 AU shown on Figure 31c as a solid red circle. *This composition is approximately the composition of the gas with which all CV3 CAIs exchanged.* This inward progressing gas exchanged with CAI phases such as perovskite and to a lesser degree melilite, leading to establishment of the CAI mixing line as shown in Figure 31d. A subsequent FU-Orionis type flare-up caused formation of pyroxene by reaction of perovskite with melilite (much of the latter still being relatively ^{16}O-rich), and the result was establishment of a more complete CAI mixing line as shown in Figure 31e. This flare-up also resulted in renewed expansion of the ^{16}O-rich "bubble" in the inner solar system, beyond 1 AU, as indicated by the red circle.

Upon return of the proto-Sun to a quiescent phase (Fig. 31f), the boundary of the ^{16}O-rich bubble again retreated to inwards of 1 AU. Finally, a possible third flare-up (Fig. 31g) caused formation of WL rims and renewed expansion of the ^{16}O-rich bubble beyond 1 AU.

An unresolved problem regarding perovskite, pyroxene, and oxygen isotopes

In most of the cases where we were able to obtain SIMS analyses, the perovskite generally has a composition that is ^{16}O-depleted, plotting (on a 3-isotope diagram) just below the intersection of the CCAM line with the terrestrial fractionation line (e.g., Figs. 3, 14). Where pyroxene is in direct contact with such perovskite, it also is ^{16}O-poor and very Ti-rich (Figs. 3, 14) – even in the WL rim where adjoining diopside is ^{16}O-rich (Fig. 9). Our model that the pyroxene formed at the expense of the perovskite rests on the petrologic and textural arguments presented in this paper, and the oxygen isotopic measurements in *16N* and *1N-b* support the model. However, the inclusion *TS19-F1* is an exception. Its perovskite is generally ^{16}O-rich, to varying degrees, and yet the pyroxene that rims it is ^{16}O-poor. There is an alternative to our model and those of Aléon (2018), and Kawasaki et al. (2018), in which the unusual isotopic compositions of Ti-rich pyroxene are a result of varying diffusion rates for oxygen within different compositions of pyroxene (Krot et al., 2021). Diffusion rates have been measured only in diopside (Ryerson and McKeegan, 1994), and the diffusion rates in Ti-Al-rich pyroxene are unknown. The question arises: what if the oxygen diffusion rates in Ti-Al-rich pyroxene are much faster than in diopside? In that case the isotopic zoning pattern in crystals such as the one in *1N-b* (illustrated in Fig. 8) is due to the interior pyroxene exchanging readily during later (parent body?) metasomatism whereas the exterior diopsidic rims exchanged little or not at all during the time span of fluid alteration. This requires fluid access to the crystal interior, presumably via fractures. This is an idea that needs to be tested experimentally by measuring oxygen diffusion rates in pyroxene of various compositions.

This latter model has a problem of its own: how did the oxygen isotopes in crystals like that in *1N-b* exchange and yet the titanium valence state (~ 50% Ti^{3+}, 50% Ti^{4+}) within the crystal remained constant? Isotope exchange involves breaking oxygen bonds, which therefore would seem to require that only tetrahedrally-coordinated oxygens were exchanged whereas octahedrally-coordinated one were not.

This decoupling of fO_2 and isotopic composition poses a problem for our model as well. Clearly the oxygen isotopic composition of the pyroxene changed significantly while the Ti^{3+}/Ti^{4+} ratio in growing pyroxene crystals remained essentially constant. If the ^{16}O-rich bubble surrounding the proto-Sun expanded and contracted as FU-Orionis flare-ups waxed and waned, an influx of outer solar system ices during the quiescent stages should have increased the oxidation state in the boundary region of the bubble to the extent that the Ti^{3+}/Ti^{4+} ratio in forming pyroxene should have decreased. This is not observed.

CONCLUSIONS

Type B CAIs formed by nebular evolution of Type A CAIs. The two types differ in both mineralogy (Type Bs contain abundant pyroxene and anorthite), bulk composition (mainly SiO_2, but not TiO_2), and textures. Formation of anorthite clearly requires the addition of silica. However, our observations suggest that pyroxene in Type A CAIs forms by reaction of perovskite with melilite. This reaction requires no addition of outside components but does require a change of redox conditions, which apparently initiates the reaction by destabilizing the perovskite and its entirely quadrivalent titanium. The textural differences between Types A and B CAIs are due to the former having been only partially melted, whereas Type B s were extensively melted and later went through near-complete liquid-line-of-descent igneous crystallization.

Prior to the onset of the pyroxene-forming reaction, any perovskite not “protected” by being enclosed in a phase such as spinel had already exchanged its oxygen isotopes with a ^{16}O poor reservoir, but neither the melilite nor any other of the phases had to any significant degree. Thus, the pyroxene that formed was initially ^{16}O-poor but, with continued reaction, the isotopic composition of the pyroxene was increasingly dominated by that of the melilite, which was still ^{16}O-rich. If melting were to continue to near completion, as in Type Bs, this isotopic zoning could be completely erased and the resulting pyroxene also would be ^{16}O-rich. It is preserved in these Type As because melting was only partial.

The observed very early isotopic exchange of perovskite is consistent with its measured oxygen diffusion coefficients, which are one to several orders of magnitude faster than those in any other CAI minerals (Robens *et al.*, 2021).

Whatever the nature and location of the isotopic reservoir with which the perovskite exchanged, that reservoir was still very reducing. The observed oxygen isotopic variations in our Type A pyroxenes were decoupled from fO_2, a finding contrary to that of J. Simon et al. (2005; 2011) in their study of WL rims. These isotopic and fO_2 conditions under which the Type A CAIs and their pyroxene formed and evolved both persisted and remained decoupled for at least 96,000 years of nebular history. However, the constancy of the fO_2 conditions poses a problem for our model that we cannot yet explain.

Our model suggests a resolution to a problem identified by Ryerson and McKeegan (1994). In Type B CAIs, pyroxene commonly is slightly less ^{16}O-rich than is spinel, and if the position of CAI minerals on the CCAM oxygen isotopic mixing line is due to post-formational exchange with an external reservoir (Clayton et al., 1977) then pyroxene must exchange more readily than does spinel. Yet Ryerson and McKeegan determined the oxygen self-diffusion coefficient for diopside pyroxene and determined it to be slower than spinel. So, in an exchange model the pyroxene should be more ^{16}O-rich – not less so – than spinel. Our results show that pyroxene initially forms by reaction of perovskite with melilite, with initial oxygen isotopic composition of the pyroxene dominated by the ^{16}O-poor composition of the perovskite and the later pyroxene composition dominated by ^{16}O-rich melilite. Type B CAIs were never completely melted, and we argue that when pyroxene-rich Type As are re-melted the ^{16}O-poor compositions of the relict pyroxenes are never entirely erased, leading to the apparent dilemma pointed out by Ryerson and McKeegan (1994).

We propose that the necessary changes in oxygen-isotope reservoirs experienced by the evolving CAIs was due to intermittent FU-Orionis flare-ups in the proto-Sun, which had the effect of alternately expanding and contracting the ^{16}O-rich region in the inner solar system. Flare-up maxima effectively expanded the ^{16}O-rich bubble, whereas during solar quiescent stages the influx of ^{16}O-poor ices from the outer solar system contracted the bubble.

The possibility that pyroxene oxygen isotope variations were caused instead by differing oxygen diffusion rates in Ti-Al-rich *vs.* Ti-Al-poor pyroxene cannot be ruled out, but this possibility can only be tested by experimental determination of oxygen diffusion rates in pyroxene of differing compositions.

Acknowledgements: Very thorough reviews by Drs. Steve Simon, Sara Russell, Associate Editor Yuri Amelin, and an anonymous reviewer, greatly improved both the content and readability of the manuscript. This work was supported by National Aeronautics and Space

Administration (NASA) grants NNX15AH68G (GJM, PI) and 14-EW14-2-0049 (ANK, PI). WiscSIMS is partly supported by National Science Foundation grants EAR03-19230 and EAR13-55590. This study was a partial contribution to research theme # 0137-2019-0002 of the Vernadsky Institute.

REFERENCES

Aléon J. (2018) Closed system oxygen isotope redistribution in igneous CAIs upon spinel dissolution. *Earth Planet. Sci. Lett.* **482**, 324–333.

Audard M., Ábrahám P., Dunham M. M., Green J. D., Grosso N., Hamaguchi K., Kastner J. H., Kóspál A., Lodato G., Romanova M. M., Skinner S. L., Vorobyov E. I., and Zhu Z. (2014) Episodic accretion in young stars *Protostars and Planets VI* (Beuther H. *et al.* editors). 363-386. University of Arizona Press.

Beckett J. R. (1986) The origin of calcium-, aluminum-rich inclusions from carbonaceous chondrites: An experimental study, p. 373. PhD Dissertation, University of Chicago

Bodénan J.-D., Starkey N. A., Russell S. S., Wright I. P., and Franchi I. A. (2014) An oxygen isotope study of Wark–Lovering rims on type A CAIs in primitive carbonaceous chondrites . *Earth Planet. Sci. Lett*. **401**: 327–336

Boss A. P., Alexander C. M. O'D., and Podolak M. (2012) Cosmochemical consequences of particle trajectories during FU Orionis outbursts by the early Sun. *Earth Planet. Sci. Lett.* **345–348**, 18–26.

Bullock E. S., Knight K. B., Richter F. M., Kita N. T., Ushikubo T., Davis A. M., MacPherson G. J., Mendybaev R. A. (2013) Evaporation conditions inferred from Mg and Si isotopic fractionation in melilite from Type B1 and B2 CAIs. *Meteorit. Planet. Sci.* **48**, 1440–1458.

Clayton R. N., Onuma N., Grossman L. and Mayeda T. K. (1977) Distribution of the pre-solar component in Allende and other carbonaceous chondrites. *Earth Planet. Sci. Lett.* **34**, 209-224.

Davis A. M., Richter F. M., Mendybaev R. A., Janney P. E., Wadhwa M. and McKeegan K. D. (2015) Isotopic mass fractionation laws for magnesium and their effects on ^{26}Al–^{26}Mg systematics in solar system materials. *Geochim. Cosmochim. Acta* **158**, 245–261.

Grossman L. (1975) Petrography and mineral chemistry of Ca-rich inclusions in the Allende meteorite. *Geochim. Cosmochim. Acta* **39**, 433–454.

Grossman L., Ebel D. S., Simon S. B., Davis A. M., Richter F. M., and Parsad N. M. (2000) Major element chemical and isotopic compositions of refractory inclusions in C3 chondrites: The separate roles of condensation and evaporation. *Geochim. Cosmochim. Acta*, 2879–2894.

Grossman L., Simon S. B., Rai V. K., Thiemens M. H., Hutcheon I. D., Williams R. W., Galy A., Ding T., Fedkin A. V., Clayton R. N., and Mayeda T. K. (2008) Primordial compositions of refractory inclusions. *Geochim. Cosmochim. Acta* **72**, 3001– 3021.

Grossman L., Beckett J. R., Fedkin A., V, Simon S. B., and Ciesla F. J. (2008) Redox conditions in the solar nebula: Observational, experimental, and theoretical constraints. In: MacPherson G, Mittlefeldht D, and Jones J (eds.) *Oxygen in the Solar System, Vol. 68: Reviews in Mineralogy and Geochemistry*, pp. 93–140. Mineralogical Society of America: Chantilly, VA.

Ireland TR (1988) Correlated morphological, chemical, and isotopic characteristics of hibonites from the Murchison carbonaceous chondrite. *Geochim. Cosmochim. Acta* **52**: 2827–2839

Ivanova M. A., Mendybaev R. A., Shornikov S. I., Lorenz C. A., and MacPherson G. J. (2021) Modeling the evaporation of CAI-like melts, and constraining the origin of CH-CB CAIs. *Geochim. Cosmochim. Acta.* **296**: 97–116.

Jacobsen, B., Yin, Q.-Z., Moynier, F., Amelin, Y., Krot, A.N., Nagashima, K., Hutcheon, I.D., Palme, H., 2008. ^{26}Al–^{26}Mg and ^{207}Pb–^{206}Pb systematics of Allende CAIs: canonical solar initial ^{26}Al/^{27}Al ratio reinstated. *Earth Planet. Sci. Lett.* **272**: 353–364.

Kawasaki N., Simon S. B., Grossman L., Sakamoto N., and Yurimoto H. (2018) Crystal growth and disequilibrium distribution of oxygen isotopes in an igneous Ca-Al-rich inclusion from the Allende carbonaceous chondrite. *Geochim. Cosmochim. Acta* **221:**318–341.

Kita N. T., Ushikubo T., Knight K. B., Mendybaev R. A., Davis A. M., Richter F. M., and Founelle J. H. (2012) Internal ^{26}Al-^{26}Mg isotope systematics of a Type B CAI: Remelting of refractory precursor solids. *Geochim. Cosmochim. Acta* **86**, 37−51.

Kita N. T., Yin Q.-Y., MacPherson G. J., Ushikubo T., Jacobsen B., Nagashima K., Kurahashi E., Krot A. N., and Jacobsen S. B. (2013). ^{26}Al-^{26}Mg isotope systematics of the first solids in the early Solar System. *Meteorit. Planet. Sci.* **48**, 1383−1400.

Krot A. N., MacPherson G. J., Ulyanov A. A., and Petaev M. I. (2004) Fine-grained, spinel-rich inclusions from the reduced CV chondrites Efremovka and Leoville: I. Mineralogy, petrology and bulk chemistry. *Meteoritics and Planetary Science* **39**: 1517–1553.

Krot A. N., Yurimoto H., Hutcheon I. D., Libourel G., Chaussidon M., Tissandier L., Petaev M. I., MacPherson G. J., Paque-Heather J., and Wark D. (2007) Type C Ca, Al-rich inclusions from Allende: Evidence for multistage formation. *Geochim. Cosmochim. Acta* **71**: 4342–4364.

Krot A. N., Nagashima K., and MacPherson G. J. (2021). On the nature of oxygen isotope heterogeneity of igneous calcium-aluminum rich inclusions in CV (Vigarano-type) carbonaceous chondrites. *84th Annual Meeting of The Meteoritical Society.* Abst. #6136.pdf

Lin Y. and Kimura M. (2003) Ca-Al-rich inclusions from the Ningqiang meteorite: Continuous assemblages of nebular condensates and genetic link to Type B inclusions. *Geochim. Cosmochim. Acta* **12:** 2251–2267.

Lorenz C., Ivanova M., Krot A., Shuvalov V. (2019) Formation of disk- and bowl-shaped igneous Ca,Al-rich inclusions: Constraints from their morphology, textures, mineralogy and modelling. *Chemie der Erde. Geochemistry* **79**: 125523.

Ludwig K. R. (2003) Isoplot 3.00 A geochronological toolkit for Microsoft Excel. *Berkeley Geochronology Center Special Publication* **No. 4**, 1–72.

MacPherson G. J. and Grossman L. (1981) A once-molten, coarse-grained, Ca-rich inclusion in Allende; *Earth Planet. Sci. Lett.* **52**: 16-24.

MacPherson GJ, Bar-Matthews M, Tanaka T, Olsen E, and Grossman L (1983) Refractory inclusions in the Murchison meteorite. *Geochim. Cosmochim. Acta* **47**: 823–839.

MacPherson G. J. and Grossman L. (1984) Fluffy Type-A inclusions in the Allende meteorite. *Geochim. Cosmochim. Acta* **48**: 29–46

MacPherson GJ, Grossman L, Hashimoto A, Bar-Matthews M, and Tanaka T (1984) Petrographic studies of refractory inclusions from the Murchison meteorite. In: Proceedings of the 15th Lunar and Planetary Science Conference, pp. C299–C312

MacPherson GJ and Davis AM (1994) Refractory inclusions in the prototypical CM chondrite, Mighei. *Geochim. Cosmochim. Acta* **58**: 5599–5625

MacPherson G. J., Petaev M. and Krot A. N. (2004) Bulk compositions of CAIs and Al-Rich chondrules: Implications of the reversal of the anorthite / forsterite condensation sequence at low nebular pressures. *Lunar Planet. Sci. Conf. XXXV* (CD ROM; #**1838**)

MacPherson G. J. and Huss G. R. (2005) Petrogenesis of Al-rich chondrules: evidence from bulk compositions and phase equilibria. *Geochim. Cosmochim. Acta* **69**: 3099–3127.

MacPherson G. J., Nagashima K., Ivanova M. A., Krot A. N. (2012a) Primary Reverse Oxygen Isotope Evolution of Pyroxene in Compact Type A CAIs from the Efremovka and NWA-3118 CV3 Chondrites: Insights into Internal CAI Mixing Lines. *43rd Lunar and Planetary Science Conference, Abstract #2415*

MacPherson G. J., Kita N. T., Ushikubo T., Bullock E. S., Davis A. M. (2012b) Well-resolved variations in formation ages for Ca-Al-rich inclusions in the early solar system. *Earth Planet. Sci. Lett.* **331**, 43−54.

McKeegan, K. D., Kallio, A. P. A., Heber, V. S., Jarzebinski, G., Mao, P. H., Coath, C. D., Kunihiro, T., Wiens, R. C., Nordholt, J. E., Moses Jr., R. W., Reisenfeld, D. B., Jurewicz, A. J. G., and Burnett, D. S., (2011) The oxygen isotopic composition of the Sun inferred from captured solar wind. *Science* **332**: 1528–1532.

Nagashima K., Krot A. N., and Huss G. R. (2015) Oxygen-isotope compositions of chondrule silicates and matrix grains in Kakangari K-grouplet chondrite. *Geochim. Cosmochim. Acta*, **151**, 49–67.

Petaev M._I. and Wood J._A. (1998) The condensation with partial isolation (CWPI) model of condensation in the solar nebula. *Meteorit. Planet. Sci.* **33**, 1123–1137.

Petaev M. I. and Wood J. A. (2005) Meteoritic constraints on temperatures, pressures, cooling rates, chemical compositions, and modes of condensation in the solar nebula. In Chondrites and the Protoplanetary Disk, vol. 341 (eds. A. N. Krot, E. R. D. Scott, and B. Reipurth). *Astronomical Society of the Pacific Conference Series*, pp. 373−407.

Richter F. M., Davis A. M., Ebel D. S., and Hashimoto A. 2002. Elemental and isotopic fractionation of type B calcium-, aluminum-rich inclusions: Experiments, theoretical considerations, and constraints on their thermal evolution. *Geochim. Cosmochim. Acta* **66**: 521–540.

Richter F. M., Janney P. E., Mendybaev R. A., Davis A. M., and Wadhwa M. (2007) Elemental and isotopic fractionation of Type B CAI-like liquids by evaporation. *Geochim. Cosmochim. Acta* **71**, 5544–5564.

Robens E., Rauschen R., Kaub J., Parras J. P., Kemp D., Freeman C. L., and De Souza R. A. (2021) Perovskite crystal symmetry and oxygen-ion transport: a molecular-dynamics study of perovskite. *Journal of Materials Chemistry* A: (DOI: 10.1039/d1ta06293j)

Ryerson F. J. and McKeegan K. D. (1994) Determination of oxygen self-diffusion in akermanite, anorthite, diopside, and spinel: implications for oxygen isotopic anomalies and the thermal histories of Ca–Al-rich inclusions. *Geochim. Cosmochim. Acta* **58**, 3713–3734.

Sakaguchi I. and Haneda H. (1996) Oxygen tracer diffusion in single-crystal $CaTiO_3$. *Journal of Solid State Chemistry* **124,** 195–197.

Sakamoto N., Seto Y., Itoh S., Kuramoto K., Fujino K., Nagashima K., Krot A. N., Yurimoto H. (2004) Remnants of the early solar system water enriched in heavy oxygen isotopes. *Science* **317**, 231−233.

Simon J. I., Young E. D., Russell S. S., Tonui E. K., Dyl K. A., Manning C. E. (2005) A short timescale for changing oxygen fugacity in the solar nebula revealed by high-resolution ^{26}Al 26Mg dating of CAI rims. *Earth Planet. Sci. Lett.* **238**, 272−283

Simon J. I., Hutcheon I. D., Simon S. B., Matzel J. E. P., Ramon E. C., Weber P. K., Grossman L., DePaolo D. J. (2011) Oxygen isotope variations at the margin of a CAI records circulation within the Solar Nebula. *Science* **331**, 1175−1178.

Simon S**.** B., Grossman L. and Davis A. M. (1991) Fassaite composition trends during crystallization of Allende Type B refractory inclusion melts. *Geochim. Cosmochim. Acta* **55**: 2635-2655.

Simon S. B., Davis A. M., and Grossman L. (1999) Origin of compact Type A refractory inclusions from CV3 carbonaceous chondrites. *Geochim. Cosmochim. Acta* **63**, 1233–1248.

Simon, S. B., and Grossman, L. (2004) A preferred method for the determination of bulk compositions of coarse-grained refractory inclusions and some implications of the results. *Geochim. Cosmochim. Acta* **68**: 4237–4248.

Simon S. B., Grossman L., Sutton S. R. (2012) Comment on "Valence state of titanium in the Wark–Lovering rim of a Leoville CAI as a record of progressive oxidation in the early Solar Nebula" by K. A. Dyl, J. I. Simon and E. D. Young. *Geochim. Cosmochim. Acta* **85**, 373–376.

Stolper E. (1982) Crystallization sequences of Ca–Al-rich inclusions from Allende: an experimental study. *Geochim. Cosmochim. Acta* **46**, 2159–2180.

Stolper E. and Paque J. (1986) Crystallization sequences of Ca–Al-rich inclusions from Allende: The effects of cooling rate and maximum temperature. *Geochim. Cosmochim. Acta* **50**: 1785– 1806.

Ushikubo T., Tenner T. J. Hiyagon H. and Kita N. T. (2017) A long duration of the ^{16}O-rich reservoir in the solar nebula, as recorded in fine-grained refractory inclusions from the least metamorphosed carbonaceous chondrites. *Geochim. Cosmochim. Acta* **201**, 103−122 Wark D. A. (1987) Plagioclase-rich inclusions in carbonaceous chondrite meteorites: liquid condensates? *Geochim. Cosmochim. Acta* **51:** 221–242.

Wark D. A. and Lovering J. F. (1977) Marker events in the early solar system: evidence from rims on Ca–Al-rich inclusions in carbonaceous chondrites. *Proc. 8th Lunar Sci. Conf.*, 95–112

Wark D. A. and Lovering J. F. (1980) More early solar system stratigraphy: Coarse-grained CAIs. *Lunar Planet. Sci. Conf. XI (abstr.),* 1208-1210.

Yamamoto D., Kawasaki N., Tachibana S., Kamibayashi M., and Yurimoto H.. (2021) An experimental study on oxygen isotope exchange reaction between CAI melt and low-pressure water vapor under simulated Solar nebular conditions. *Geochim. Cosmochim. Acta* **314**: 108– 120

Yoneda S. and Grossman L. (1995) Condensation of $CaO–MgO–Al_2O_3–SiO_2$ liquids from cosmic gases. *Geochim. Cosmochim. Acta* **59**, 3413–3444

Yurimoto H., Ito M., and Nagasawa H. (1998) Oxygen isotope exchange between refractory inclusion in Allende and solar nebula gas. *Science* **282**, 1874–1877.

Yurimoto H., Nagashima K., and Kunihiro T. (2003) High precision isotope micro-imaging of materials. *Appl. Surf. Sci.* **203**, 793−797.

Table 1. Oxygen isotope compositions of CAIs

CAI	Spot #	$\delta^{18}O$	2σ	$\delta^{17}O$	2σ	$\Delta^{17}O$	2σ	Notes
3138-F8	Area 4 Mel #2	2.2	1.3	-4.9	1.6	-6.1	1.7	
3138-F8	Area 4 Mel #3	3.2	1.3	-3.1	1.6	-4.8	1.8	
3138-F8	Area 4 Mel #4	2.6	1.3	-3.4	1.6	-4.8	1.8	
3138-F8	Area 1 Mel #6	-10.5	0.7	-16.1	0.8	-10.6	0.8	
3138-F8	Area 1 Mel #8	-11.1	0.7	-15.9	0.7	-10.2	0.8	
3138-F8	Area 3 Me1 #1	2.5	0.6	-3.1	0.8	-4.4	0.8	
3138-F8	Area 3 Me1 #2	2.8	0.5	-3.5	0.7	-4.9	0.8	
3138-F8	Area 2 Mel #8	2.3	0.6	-3.6	0.8	-4.8	0.8	
3138-F8	Area 7 Mel #1	-6.0	0.6	-10.8	0.7	-7.6	0.8	
3138-F8	Area 7 Mel #2	1.4	0.5	-4.7	0.8	-5.4	0.8	
3138-F8	Area 4 Mel #1	0.5	0.5	-5.0	0.8	-5.3	0.8	
3138-F8	Area 14 Mel-1	-6.5	1.0	-11.8	1.9	-8.4	1.9	near WLR
3138-F8	Area 14 Mel-2	0.0	1.0	-5.9	2.0	-6.0	2.1	near WLR
3138-F8	Area 15 Mel-3	-17.4	1.2	-20.1	1.9	-11.1	2.0	near WLR
3138-F8	Area 15 Mel-4	-15.4	1.1	-17.4	1.9	-9.4	2.0	near WLR
3138-F8	Area 13 Mel-5	-9.1	1.0	-14.0	1.6	-9.3	1.7	near WLR
3138-F8	Area 5 Hib #1	-41.7	1.3	-44.5	1.6	-22.8	1.7	
3138-F8	Area 16 Pv-2	-7.8	0.7	-11.8	1.7	-7.7	1.7	near WLR
3138-F8	Area 16 Pv-2	1.9	-0.6					corrected for Sp
3138-F8	Area 2 Pyx #1	8.4	0.5	1.8	1.5	-2.6	1.5	
3138-F8	Area 4 Pyx #1	5.1	1.2	-1.5	0.9	-4.1	1.1	
3138-F8	Area 3 Pyx #1	7.7	1.2	0.9	0.9	-3.1	1.1	
3138-F8	Area 15 Pyx-2	-50.0	1.3	-48.9	2.7	-22.9	2.8	near WLR
3138-F8	Area 13 Pyx-3	-48.2	1.3	-48.0	2.9	-22.9	3.0	near WLR
3138-F8	Area 13 Pyx-4	-46.2	1.4	-46.4	2.9	-22.3	3.0	near WLR
3138-F8	Area 2 Sp #1	-41.9	1.3	-44.9	1.6	-23.1	1.8	
3138-F8	Area 4 Sp #1	-40.1	1.3	-43.8	1.7	-23.0	1.8	
1N-b	Area 2 Mel #1	6.0	0.9	0.8	1.1	-2.3	1.2	
1N-b	Area 2 Mel #2	6.6	0.9	1.0	1.1	-2.4	1.2	
1N-b	Area 2 Mel #3	6.6	0.9	0.9	1.1	-2.5	1.2	
1N-b	Area 2 Mel #4	7.0	0.9	0.9	1.1	-2.7	1.2	
1N-b	Area 2 Mel #5	6.2	0.9	0.4	1.1	-2.9	1.2	
1N-b	Area 4 Mel #6	7.0	0.9	1.0	1.1	-2.6	1.2	
1N-b	Area 4 Mel #7	5.6	0.9	0.5	1.1	-2.4	1.2	
1N-b	Area 4 Mel #8	4.3	0.9	-0.6	1.1	-2.8	1.2	
1N-b	Area 3 Mel #9	3.2	1.0	-1.6	1.1	-3.2	1.2	
1N b	Area 3 Mel #10	3.1	0.9	-1.2	1.1	-2.8	1.2	
1N b	Area 3 Mel #11	-6.4	0.9	-10.7	1.2	-7.4	1.3	
1N b	Area 3 Mel #12	2.5	0.9	-2.2	1.1	-3.5	1.2	
1N b	Area 1 Mel #13	2.8	1.0	-2.1	1.2	-3.6	1.3	
1N b	Area 1 Mel #14	3.7	1.0	-1.1	1.2	-3.0	1.3	
1N b	Area 1 Mel #15	-1.0	1.0	-4.9	1.2	-4.4	1.3	
1N b	Area 1 Mel #16	1.5	1.0	-3.0	1.2	-3.8	1.3	
1N b	Area 4 Pyx #1	-8.7	0.8	-12.7	1.0	-8.1	1.1	
1N b	Area 4 Pyx #2	-10.1	0.8	-14.2	1.1	-8.9	1.1	
1N b	Area 4 Pyx #3	-38.9	0.8	-41.7	1.0	-21.5	1.1	
1N b								

Area 4 Pyx #4-44.0 0.9-46.2 1.0-23.3 1.1 *1N b* Area 4 Pyx #5-35.5 0.8-37.8 1.0-19.4 1.1 *1N b* Area 4 Pyx #6-15.5 0.8-19.8 1.0-11.7 1.1 *1N b* Area 4 Pyx #7-4.8 0.8-9.2 1.0-6.6 1.1 *1N b* Area 4 Pyx #8-36.5 0.8-40.1 1.1-21.1 1.2 *1N b* Area 3 Pyx #9 5.9 0.8 0.4 1.1-2.6 1.2 *1N b* Area 2 Pyx #10-17.9 0.8-23.1 1.1-13.7 1.2 *1N b* Area 2 Pyx #11-41.3 0.8-44.3 1.0-22.9 1.1 *1N b* Area 3 Pyx #13-14.9 1.0-20.1 1.0-12.3 1.1 WLR

1N b Area 3 Pyx #14-12.8 1.0-18.1 1.2-11.5 1.3 WLR *1N b* Area 4 Sp #1-43.1 1.2-44.7 0.9-22.3 1.1 *1N b* Area 4 Sp #2-44.4 1.2-46.3 0.9-23.2 1.1 *1N b* Area 2 Sp #3-41.8 1.2-44.6 0.9-22.9 1.1 *1N b* Area 2 Sp #4-43.1 1.2-45.9 0.9-23.4 1.1

16N Area 2 An #1-17.3 1.0-21.1 1.1-12.1 1.3 *16N* Area 2 An #2-12.9 1.0-16.9 1.1-10.2 1.2 *16N* Area 3 An #3-6.7 1.0-11.9 1.1-8.3 1.2 *16N* Area 8 An #4-21.5 1.0-24.9 1.1-13.7 1.2 *16N* Area 8 An #5-0.5 1.0-5.1 1.2-4.8 1.3 *16N* Area 8 An #6-14.3 1.0-18.2 1.2-10.7 1.3 *16N* Area 2 Mel #1 2.0 1.0-1.7 0.9-2.7 1.0 *16N* Area 2 Mel #2 2.3 1.1-1.4 0.9-2.6 1.1 *16N* Area 2 Mel #3 1.8 1.0-1.6 0.9-2.5 1.1 *16N* Area 2 Mel #4 2.3 1.1-1.6 0.9-2.8 1.1 *16N* Area 2 Mel #5 1.6 1.1-1.7 0.9-2.6 1.0 *16N* Area 3 Mel #6 2.3 1.0-1.6 0.9-2.8 1.1 *16N* Area 3 Mel #7 1.5 1.1-1.4 0.9-2.2 1.1 *16N* Area 4 Mel #8 0.2 1.0-3.3 0.9-3.3 1.1 *16N* Area 4 Mel #9 1.2 1.0-2.3 1.0-2.9 1.1 *16N* Area 9 Mel #10 1.6 1.0-2.1 0.9-2.9 1.1

16N Area 5 Mel #11 -0.1 1.1 -2.6 0.9 -2.6 1.0 *16N* Area 5 Mel #12 -0.7 1.0 -5.6 0.9 -5.3 1.0 *16N* Area 1 Mel #13 1.7 1.0 -3.8 0.9 -4.7 1.0 *16N* Area 1 Mel #14 1.0 1.0 -3.9 0.9 -4.4 1.1 *16N* Area 1 Mel #15 1.7 1.0 -2.6 0.9 -3.5 1.1 *16N* Area 1 Sp #2 -42.8 1.0 -45.4 0.9 -23.1 1.0 *16N* Area 1 Sp #3 -39.9 1.0 -44.2 0.9 -23.4 1.0 *16N* Area 4 Sp #4 -43.4 1.0 -45.5 0.9 -22.9 1.0 *16N* Area 4 Sp #5 -44.8 1.0 -46.2 0.8 -22.8 1.0 *16N* Area 4 Sp #6 -44.1 1.0 -46.1 0.9 -23.1 1.0 *16N* Area 1 Pv #1 4.6 1.0 0.2 0.8 -2.2 1.0 *16N* Area 2 Pyx #1 -39.2 0.9 -41.4 1.0 -21.0 1.1 *16N* Area 2 Pyx #2 -34.5 1.0 -37.0 1.0 -19.1 1.1 *16N* Area 2 Pyx #3 -25.0 0.9 -28.7 1.0 -15.7 1.1 *16N* Area 4 Pyx #8 -24.8 0.9 -28.2 1.0 -15.3 1.1 *16N* Area 4 Pyx #9 -38.4 0.9 -41.1 1.0 -21.1 1.1 *16N* Area 4 Pyx #10 -11.4 0.9 -15.2 1.0 -9.3 1.1 *16N* Area 4 Pyx #11 -15.7 0.9 -19.8 1.0 -11.7 1.1 *16N* Area 4 Pyx #12 -4.7 0.9 -8.9 1.0 -6.5 1.1 *16N* Area 4 Pyx #13 -6.8 0.9 -11.3 0.9 -7.8 1.1 *16N* Area 7 Pyx #14 -38.9 0.9 -42.4 1.0 -22.2 1.1 *16N* Area 7 Pyx #15 -35.1 0.9 -38.5 1.0 -20.3 1.1 *16N* Area 7 Pyx #16 -19.8 0.9 -24.9 1.0 -14.6 1.1 *16N* Area 11 Pyx #17 6.9 0.9 0.0 1.1 -3.5 1.2 *16N* Area 11 Pyx #18 6.1 0.9 -0.7 1.0 -3.9 1.1 *16N* Area 11 Pyx #19 6.7 0.9 0.2 1.1 -3.3 1.2 *16N* Area 5 Pyx #4 2.1 0.9 -2.1 1.0 -3.2 1.1 near Pv

16N Area 4 Pyx #7 3.3 0.9 -2.8 1.0 -4.5 1.1 near Pv *16N* Area 5 Pyx #5 -44.4 0.9 -46.4 1.0 -23.3 1.1 WLR *16N* Area 5 Pyx #6 -39.3 0.9 -42.1 1.0 -21.6 1.1 WLR

TS19-F1 Area 4 Mel #1 3.1 0.5 -1.2 0.5 -2.8 0.5 15 μm spot *TS19-F1* Area 4 Mel #2 2.5 0.5 -1.5 0.5 -2.9 0.4 15 μm spot *TS19-F1* Area 4 Mel #3 3.1 0.5 -1.2 0.5 -2.8 0.5 15 μm spot *TS19-F1* Area 3 Mel #4 3.0 0.5 -1.2 0.5 -2.8 0.5 15 μm spot *TS19-F1* Area 3 Mel #5 3.0 0.5 -1.2 0.5 -2.8 0.5 15 μm spot *TS19-F1* Area 7 Mel #6 3.1 0.5 -1.3 0.5 -2.9 0.5 15 μm spot *TS19-F1* Area 7 Mel #7 3.3 0.6 -1.1 0.5 -2.8 0.5 15 μm spot *TS19-F1* Area 6 Mel #8 4.2 0.5 -0.6 0.5 -2.8 0.5 15 μm spot *TS19-F1* Area 6 Mel #9 3.7 0.6 -0.8 0.5 -2.7 0.5 15 μm spot *TS19-F1* Area 8 Mel #10 3.9 0.5 -0.8 0.5 -2.8 0.5 15 μm spot

TS19-F1 Area 4 Sp #1 -45.7 0.7 -47.7 0.5 -23.9 0.4 15 μm spot *TS19-F1* Area 3 Sp #2 -45.3 0.7 -47.5 0.4 -24.0 0.4 15 μm spot *TS19-F1* Area 7 Sp #3 -45.5 0.7 -47.6 0.4 -23.9 0.4 15 μm spot

TS19-F1 Area 8 Sp #4 -45.1 0.7 -47.7 0.4 -24.3 0.4 15 μm spot *TS19-F1* Area 4 Pv #1 -40.2 0.6 -40.8 0.6 -19.9 0.5 15 μm spot *TS19-F1* Area 4 Pv #2 -37.1 0.6 -38.0 0.6 -18.7 0.6 15 μm spot *TS19-F1* Area 4 Pv #3 -39.7 0.6 -40.4 0.6 -19.7 0.5 15 μm spot *TS19-F1* Area 4 Pv #4 -38.1 0.6 -38.8 0.6 -19.0 0.5 15 μm spot *TS19-F1* Area 3 Pv #1 -34.7 2.5 -34.2 2.7 -16.2 2.4 3 μm spot *TS19-F1* Area 3 Pv #2 -46.3 2.5 -47.0 3.0 -23.0 2.7 3 μm spot *TS19-F1* Area 3 Pv #3 -45.7 2.6 -47.0 2.8 -23.2 2.5 3 μm spot

TS19-F1 Area 3 Pv #4 -23.6 2.5 -24.9 2.8 -12.6 2.5 3 μm spot *TS19-F1* Area 3 Pv #5 -34.6 2.6 -33.9 3.0 -15.9 2.7 3 μm spot *TS19-F1* Area 3 Pv #6 -24.9 2.6 -26.0 2.8 -13.0 2.6 3 μm spot *TS19-F1* Area 6 Pv #7 -42.5 2.5 -44.6 2.8 -22.5 2.6 3 μm spot *TS19-F1* Area 6 Pv #8 -47.9 2.6 -47.2 3.2 -22.4 2.9 3 μm spot *TS19-F1* Area 6 Pv #9 -32.9 2.5 -33.4 2.8 -16.3 2.6 3 μm spot *TS19-F1* Area 7 Pyx #1 -46.9 2.1 -48.3 2.2 -23.9 2.4 3 μm spot, incl in pv

TS19-F1 Area 6 Pyx #2 -35.5 2.1 -37.9 2.2 -19.5 2.5 3 μm spot, incl in pv *TS19-F1* Area 3 Pyx #3 0.6 2.1 -2.6 2.2 -2.9 2.5 3 μm spot, rim on pv *TS19-F1* Area 3 Pyx #4 0.9 2.1 -2.7 2.1 -3.1 2.4 3 μm spot, rim on pv *TS19-F1* Area 3 Pyx #5 1.1 2.1 -1.2 2.0 -1.8 2.3 3 μm spot, rim on pv *TS19-F1* Area 4 Pyx #6 0.4 2.1 -2.8 2.1 -3.0 2.4 3 μm spot, rim on pv *TS19-F1* Area 6 Pyx #7 -43.8 2.0 -46.4 2.3 -23.6 2.6 3 μm spot, incl in pv *TS19-F1* Area 6 Pyx #8 -42.4 2.1 -45.7 2.3 -23.7 2.5 3 μm spot, incl in pv *TS19-F1* Area 8 Pyx #9 -40.1 2.1 -44.4 2.6 -23.5 2.8 3 μm spot, incl in pv *TS19-F1* Area 8 Pyx #10 -41.9 2.1 -43.8 2.3 -22.0 2.5 3 μμ spot, incl in pv

Table 2. Al-Mg isotope compositions of CAIs

CAI Phase, spot # ^{27}Al/^{24}Mg 2σ δ^{26}Mg* 2 s

1N-b Mel #17 2.23 0.02 0.77 0.09 *1N-b* Mel #18 6.46 0.06 2.36 0.12 *1N-b* Mel #19 5.24 0.05 1.79 0.12 *1N-b* Mel #20 13.41 0.14 4.80 0.23 *1N-b* Mel #21 10.36 0.10 3.58 0.15 *1N-b* Mel #22 5.17 0.05 1.86 0.12 *1N-b* Mel #23 9.21 0.09 3.26 0.15 *1N-b* Mel #24 8.59 0.09 3.04 0.13 *1N-b* Mel #25 22.55 0.24 7.75 0.25 *1N-b* Mel #26 3.66 0.04 1.34 0.08 *1N-b* Pyx #15 1.81 0.02 0.69 0.06 *1N-b* Pyx #16 1.95 0.02 0.72 0.05 *1N-b* Pyx #17 2.54 0.03 0.94 0.06 *1N-b* Pyx #18 1.91 0.02 0.71 0.05 *1N-b* Pyx #19 2.99 0.03 1.10 0.07 *1N-b* Pyx #20 2.10 0.02 0.80 0.05 *1N-b* Pyx #21 1.83 0.02 0.70 0.05 *1N-b* Pyx #22 2.58 0.03 0.93 0.06 *1N-b* Pyx #23 2.74 0.03 0.96 0.07 *1N-b* Pyx #24 2.87 0.03 0.99 0.07 *1N-b* Sp #6 2.52 0.03 0.97 0.07 *1N-b* Sp #7 2.54 0.03 0.95 0.07

(^{26}Al/^{27}Al)0 = 4.81 ± 0.11 × 10^{-5}
MSWD = 0.7 (δ^{26}Mg)$_0$ = 0.06 ± 0.03

16N Mel #16 18.04 0.19 6.58 0.18 *16N* Mel #17 36.80 0.49 13.59 0.37 *16N* Mel #18 15.64 0.25 5.89 0.21 *16N* Mel #19 5.46 0.05 2.10 0.09 *16N* Mel #20 6.93 0.07 2.35 0.12 *16N* Mel #21 7.68 0.08 2.65 0.12 *16N* Mel #22 4.13 0.04 1.64 0.09 *16N* Mel #23 4.05 0.04 1.61 0.09 *16N* Mel #24 6.76 0.07 2.48 0.10 *16N* Pyx #20 2.72 0.03 0.91 0.08 *16N* Pyx #21 2.66 0.03 0.86 0.08 *16N* Pyx #22 3.96 0.04 1.34 0.08 *16N* Pyx #23 2.72 0.03 0.88 0.08 *16N* Pyx #24 2.75 0.03 0.92 0.08
16N Pyx #25 3.80 0.04 1.39 0.08 *16N* Pyx #26 3.32 0.03 1.14 0.08 *16N* Pyx #27 2.54 0.03 0.86 0.08 *16N* Sp #7 2.57 0.03 0.91 0.07 *16N* Sp #8 2.57 0.03 0.93 0.07 *16N* Sp #9 2.56 0.03 1.02 0.07 *16N* Sp #10 2.56 0.03 0.96 0.07 *16N*[1] An #1 341 7 93 5

16N[1] An #2 652 13 180 8 *16N*[1] An #3 537 10 120 6 *16N*[1] An #4 303 6 123 4 *16N*[1] An #5 445 8 139 5 *16N*[1] An #6 243 4. 82 3 *16N*[1] An #7 417 8 132 5 *16N*[1] An #8 449 9 99 5 *16N*[1] An #9 701 14 99 7 *16N*[1] An #10 674 13 175 6 (^{26}Al/^{27}Al)0 = 5.15 ± 0.10

$\times 10^{-5}$

MSWD = 3.9 $(\delta^{26}Mg)_0 = -0.04 \pm 0.03$

TS-19	Mel #1	27.60	0.28	9.92	0.34
TS-19	Mel #2	16.64	0.21	5.75	0.24
TS-19	Mel #3	8.54	0.09	3.36	0.16
TS-19	Mel #4	19.31	0.19	6.92	0.25
TS-19	Mel #5	4.51	0.05	1.73	0.11
TS-19	Mel #6	3.99	0.04	1.69	0.10
TS-19	Mel #7	4.99	0.05	1.87	0.11
TS-19	Mel #8	5.23	0.05	2.02	0.14
TS-19	Sp #1	2.52	0.03	1.09	0.06
TS-19	Sp #2	2.51	0.03	1.02	0.06
TS-19	Sp #3	2.51	0.03	1.03	0.05

$(^{26}Al/^{27}Al)_0 = 4.89 \pm 0.12 \times 10^{-5}$

MSWD = 2.3 $(\delta^{26}Mg)_0 = 0.17 \pm 0.04$

1623-11	Mel#1	10.39	0.12	3.82	0.15
1623-11	Mel#2	8.85	0.09	3.20	0.12
1623-11	Mel#3	10.03	0.10	3.61	0.14
1623-11	Mel#4	1.92	0.02	0.80	0.11
1623-11	Mel#5	1.08	0.01	0.46	0.11
1623-11	Mel#6	8.54	0.09	3.04	0.16
1623-11	Mel#7	2.33	0.02	0.87	0.11
1623-11	Mel#8	9.14	0.09	3.26	0.14
1623-11	Mel#9	8.77	0.10	3.26	0.16
1623-11	Px#1	2.22	0.02	0.73	0.06
1623-11	Px#2	2.06	0.02	0.70	0.05
1623-11	Px#3	3.47	0.04	1.12	0.06
1623-11	Px#4	2.10	0.02	0.65	0.06
1623-11	Px#5	3.24	0.03	1.09	0.06
1623-11	Px#6	3.11	0.03	1.07	0.07
1623-11	Px#7	2.08	0.02	0.63	0.06
1623-11	Sp#1	2.72	0.03	1.01	0.07
1623-11	Sp#2	2.60	0.03	0.95	0.07
1623-11	Sp#3	2.61	0.03	0.94	0.07
1623-11	An#2	294	6	103	3
1623-11	An#3	280	5	97	3
1623-11	An#4	918	19	324	7
1623-11	An#5	626	12	218	5

$(^{26}Al/^{27}Al)_0 = 4.94 \pm 0.07 \times 10^{-5}$

MSWD = 2.8 $(\delta^{26}Mg)_0 = -0.03 \pm 0.02$

[1] Not included in regression

Table 3. Average compositions of small pyroxene grains in *16N, 1N-b, TS19-F1,* and *3138-F8*

	16N	*1N-b*	*3138-F8*	*TS19-F1*
	average	average	average	average
	N=6	N=4	N=22	N=10
SiO_2	28.37	28.04	29.38	32.36
Al_2O_3	23.50	23.48	23.34	20.20
FeO	0.02	0.02	0.05	0.05
MgO	4.05	4.58	4.82	6.73
CaO	24.38	25.17	25.02	25.13
TiO_2^{*}	18.12	19.24	17.79	13.23
$[TiO_2]^{**}$	4.90	7.66	6.20	6.26
$[Ti_2O_3]^{**}$	11.90	10.42	10.43	6.27
Cr_2O_3	0.04	0.04	0.01	0.09
TOTAL	98.48	100.57	100.41	97.79
[TOTAL]	97.16	99.41	99.25	97.09

Cations per 6 Oxygens

Si	1.114	1.078	1.127	1.254
Al(IV)	0.886	0.922	0.873	0.746
Σ TET.	2.000	2.000	2.000	2.000
Al(VI)	0.201	0.142	0.181	0.177
Mg	0.237	0.263	0.275	0.389
Fe	0.001	0.001	0.002	0.002
Ti^{4+}	0.145	0.222	0.179	0.182
Ti^{3+}	0.390	0.335	0.334	0.203
Σ OCT.	0.976	0.963	0.972	0.956
Ca	1.026	1.037	1.028	1.043
TOTAL	4.002	4.001	4.000	3.999

[*] TiO_2 – Total Ti expressed as TiO_2

[**] – Ti^{4+}, Ti^{3+} calculated by stoichiometry assuming 4 cations per formula unit.

Fig. 1. BSE image (top) and Ca-Al-Mg element map (bottom) of *3138-F8*. The fragment at left, set off with the yellow dotted line, is not part of the same CAI. Except where specifically noted otherwise, in this and all subsequent element maps red = Mg, blue = Al, green = Ca. Abbreviations: Mel – melilite; Sp – spinel; Hib – hibonite; Pyx – pyroxene; Mtx – meteorite matrix.

Fig. 2. Detailed BSE image (top) and Si-Ti element map (bottom) of a portion of *3138-F8*, showing Ti-rich pyroxene (Ti-Pyx; yellow) mantling a group of small perovskite (Pv; orange) crystals. In this image perovskite is orange, pyroxene is yellow, and melilite is green. Other abbreviations as used previously

Fig. 3. Oxygen isotopic compositions of phases in *3138-F8*. Spinel and hibonite are ^{16}O -rich, melilite is variably depleted in ^{16}O, and perovskite is $\delta^{18}O$ -poor. Interior pyroxene (Int Pyx) is depleted in ^{16}O, whereas diopside in the WL rim (WLR Diop) is ^{16}O -rich. “Pv meas” is the measured perovskite composition that includes about 25% beam overlap onto spinel. “Pv corr” is the calculated composition of pure perovskite. In this and all subsequent isotope charts, all data points are plotted with 2σ error bars. Where not visible, the error bars are smaller than the plotting symbol. Other abbreviations as used previously.

Fig.4. Al-Mg isotope diagram for *3138-F8*. All phases plot close to a single isochron. Data from, and figure modified from, MacPherson et al. (2012). Abbreviations as used previously.

Fig. 5. BSE image (top) and Ca-Al-Mg element map (bottom) of *1N-b*. Abbreviations as used previously.

Fig. 6. Enlarged BSE image (top) and Ca-Al-Mg element map (bottom) of a portion of *1N-b*. Melilite in immediate contact with pyroxene is magnesium-rich (greenish blue) relative to melilite elsewhere (blue). The pyroxene crystals show clear compositional zoning, with light Ti rich cores and darker Ti-poor rims. Abbreviations as used previously.

Fig. 7. Oxygen isotopic compositions of phases in *1N-b*. Spinel is uniformly ^{16}O -rich, anorthite is variably depleted in ^{16}O, and melilite is uniformly ^{16}O -poor. Ti-rich pyroxene in the WL rim is depleted in ^{16}O. Interior (igneous) pyroxene spans the entire range of isotopic compositions. Abbreviations as used previously.

Fig. 8. BSE image, oxygen isotope profile, and titanium compositional profile across a zoned pyroxene crystal in *1N-b*. The white dotted line marks the location of the titanium compositional profile, and the thick white line and large white circles show the locations of the SIMS oxygen isotopic profile. The dark margin of the crystal is Ti- and Al-poor, and the lighter core is enriched in both elements; the ratio of Ti^{3+} to Ti^{4+} is approximately constant across the crystal. The oxygen isotopic composition varies drastically across the crystal, with the Ti-rich core being ^{16}O -poor and the Ti-poor crystal rim being ^{16}O-rich.

Fig. 9. BSE images and isotopographs of a portion of 1Nb. (a) Two generations of perovskite are visible in this BSE image, one in the outer CAI margin and a second generation within the WL rim; (b) enlarged BSE and (c) Mg-Si-Ti images corresponding to the white square outline in (a). Note that there is a sharp distinction between the outer diopside rim layer (bright green) and the inner Ti-rich pyroxene rim layer (bluish-green). The yellow circle outlines the region shown in (d) and (e) , which are respectively $^{27}Al^-/^{16}O^-$and ^{18}O SCAPS images, showing that the Ti-rich pyroxene and perovskite are ^{18}O-rich (^{16}O -poor) whereas the spinel and diopside are ^{18}O-poor (^{16}O -rich). Abbreviations as used previously.

Fig.10 Al-Mg isotope diagram for *1N-b*. All phases define an exceptionally well-constrained isochron. Abbreviations as used previously.

Fig. 11. BSE image (top) and Ca-Al-Mg element map (bottom) of *16N*. Abbreviations as used previously except: An – anorthite

Fig. 12. Enlarged BSE images (top) and Ca-Al-Mg element maps (bottom) of two regions of *16N*. In (a) and (b), melilite in immediate contact with anorthite and pyroxene is magnesium-rich (green) relative to melilite elsewhere (blue). In (c) and (d), pyroxene crystals poikilitically enclose smaller tabular but rounded melilite crystals Abbreviations as used previously except: Poik. Pyx. – poikilitic pyroxene.

Fig. 13. Paired BSE and cathodoluminescence images of an anorthite region in *16N*, with the latter showing anorthite (shades of blue) and spinel (orange). The cathodoluminescence image mimics the polysynthetic twinning of the feldspar, and the continuity shown here demonstrates that this irregular grain is in fact a single crystal of probable igneous origin. Abbreviations as used previously.

Fig. 14. Oxygen isotopic compositions of phases in *16N*. Spinel is ^{16}O -rich, as is diopside in the WL rim. Anorthite is variably depleted in ^{16}O, and melilite and perovskite are ^{16}O -poor. Interior

(igneous) pyroxene spans nearly the entire range of isotopic compositions in this CAI. The Ti rich portions of large zoned crystals are ^{16}O -poor, and the Ti-depleted portions of the same crystals are ^{16}O -rich. Abbreviations as used previously.

Fig. 15. Graph showing the correlation between total TiO_2 content of pyroxene in 16N and Δ^{17}O. Small Δ^{17}O means ^{16}O -depletion, so the most Ti-rich pyroxene is the most ^{16}O -depleted.

Fig.16. Detailed BSE image of a portion of NWA16N showing the textural relationships between perovskite grains and anastomosing pyroxene that is forming at the expense of the perovskite. The numbers in the white squares give the Δ^{17}O values for the pyroxene marked by the white circles, which clearly is very ^{16}O -depleted. Note that the electron albedo (brightness) of the pyroxene decreases with distance away from the perovskite, indicating that the TiO_2 content is decreasing. No electron microprobe analyses were obtained for these pyroxenes, so the marked spots are not represented on Fig. 15. Abbreviations as used previously.

Fig.17 Al-Mg isotope diagram for *16N*. Melilite, pyroxene, and spinel yield a well-defined isochron, with only the two most Mg-rich melilite points and one pyroxene point plotting more than 2σ away from the correlation line. Anorthite mostly is disturbed and scatters away from the isochron. For this reason, anorthite was not included in the regression for the isochron. Abbreviations as used previously.

Fig. 18. BSE image (top) and Ca-Al-Mg element map (bottom) of Vigarano *1623-11*. Although texturally a Compact Type A CAI, this object contains abundant anorthite and pyroxene. Had it mostly melted and resolidified, it would be considered a Type B. Abbreviations as used previously.

Fig. 19. Detailed BSE images (top) and Ca-Al-Mg element maps (bottom) of two regions within *1623-11*. Figures (a) and (b) show a eutectic-like assemblage of magnesium-rich melilite, pyroxene, anorthite, and spinel. Note that the anorthite occurs as anastomosing irregular regions that enclose euhedral tablets of aluminum-rich melilite. The color scale of the lower image has been greatly stretched to emphasize the difference between aluminum-rich and magnesium-rich melilite (light blue and lime green, respectively. For this reason, the spinel appears red rather than the more usual magenta in this kind of element map. Figures (c) and (d) show even more clearly the highly irregular nature of the anorthite crystals that enclose tabular melilite crystals. Abbreviations as used previously except: Åk – åkermanite.

Fig. 20. BSE image (top) and cathodoluminescence map (bottom) of anorthite crystals in *1623-11.* The luminescence map mimics the polysynthetic twinning of the plagioclase and shows that this large irregular region in fact consists of coarse-grained single crystals. Abbreviations as used previously.

Fig. 21 – Al-Mg isotope diagrams for *1623-11*: (a) spinel, melilite, and pyroxene; and (b) anorthite. The two isochrons are well defined, are within error of each other, and show no evidence of disturbance. The slope given in the top figure is for all phases combined.

Fig. 22. BSE image (top) and Ca-Al-Mg element map (bottom) of Allende *TS19-F1*. Abbreviations as used previously.

Fig. 23. Detailed BSE images of *TS19-F1*, showing the occurrences of perovskite as large irregular crystals in the inclusion core (top) and as small grains near the inclusion margin (bottom). Abbreviations as used previously.

Fig. 24. Detailed BSE images of *TS19-F1*, showing the occurrence of titanium-rich pyroxene as thin rims on perovskite (a, b) and as tiny inclusions in perovskite and spinel (c, d). Abbreviations as used previously.

Fig. 25. Oxygen isotopic compositions of phases in *TS19-F1*. Spinel is ^{16}O -rich, melilite is uniformly depleted in ^{16}O, and perovskite is variably depleted in ^{16}O. Pyroxene enclosed within perovskite is ^{16}O-rich whereas pyroxene rims on perovskite are ^{16}O-depleted

Fig. 26. Al-Mg isotope diagram for *TS19-F1*. Melilite and spinel yield a well-defined isochron. Abbreviations as used previously.

Fig. 27. Comparison of initial ^{26}Al/^{27}Al ratios for the five studied Type A CAIs. The spread in values corresponds to a maximum age difference of approximately 96,000 years. The dashed line marks the Solar system initial value of 5.23×10^{-5}(Jacobsen *et al*., 2008)

Fig. 28. Bulk compositions of the studied CAIs plotted on the ternary liquidus system gehlenite anorthite-forsterite, as projected from spinel (Stolper, 1982). Fields are labeled according to their liquidus phase, plus spinel (Sp) plus liquid (L). Most of the inclusions, including the pyroxene rich objects *1N-b* and *16N*, plot in the general region occupied by Type A CAIs) ("A"). Only the anorthite-rich inclusion *1623-11* plots in the region occupied by Type B CAIs ("B"), demonstrating that the main bulk compositional difference between Types A and B CAIs is due to the addition of silica (see text).

Fig. 29. Histogram of bulk TiO_2 contents in Types A and B CAIs, showing nearly complete overlap between the two CAI varieties. A slight tendency for Type Bs to be richer in TiO_2 (at the 0.2-0.4 wt. % level) may be due to the fact that the small perovskite grains in Type As are easier to be missed (hence, under-represented) relative to pyroxene during manual point counting. This difference is not seen when using quantitative electron compositional mapping. Data from Beckett (1986), Simon and Grossman (2004), and Ivanova *et al.* (2021).

Fig. 30. Detailed BSE image of a portion of another Fluffy Type A CAI, Vigarano *477-5*. Veins of anorthite and diopside (Di) cross-cut regions within the interior of the CAI. The monomineralic nature of these thin bands suggest reaction between the solids and infiltrating nebular gas. Melting and re-crystallization of such veins would lead to the formation of igneous anorthite and pyroxene such as seen in Compact Type As like the ones studied herein. The kirschsteinite (Kir) is a later product of parent body alteration. Other abbreviations as used previously.

Fig. 31. Schematic model showing how intermittent FU-Orionis outbursts lead to a fluctuation of the ^{16}O-rich bubble surrounding the proto-Sun. During quiescent periods between outbursts, rapid exchange of perovskite relative to other CAI phases sets up the formation of ^{16}O -depleted pyroxene during a subsequent FU-Orionis outburst. The pyroxene forms by reaction of the perovskite with melilite, and the reaction is triggered by a change in redox conditions. See text for details.

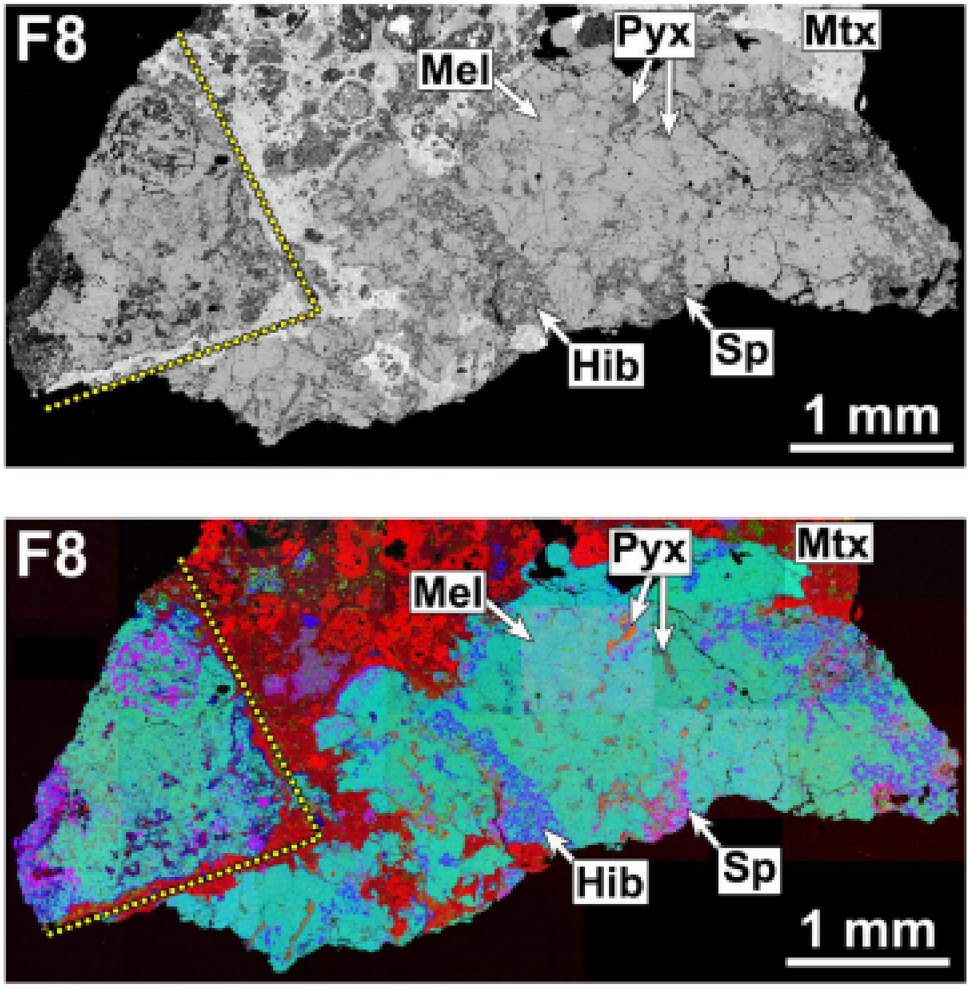

Figure 1.

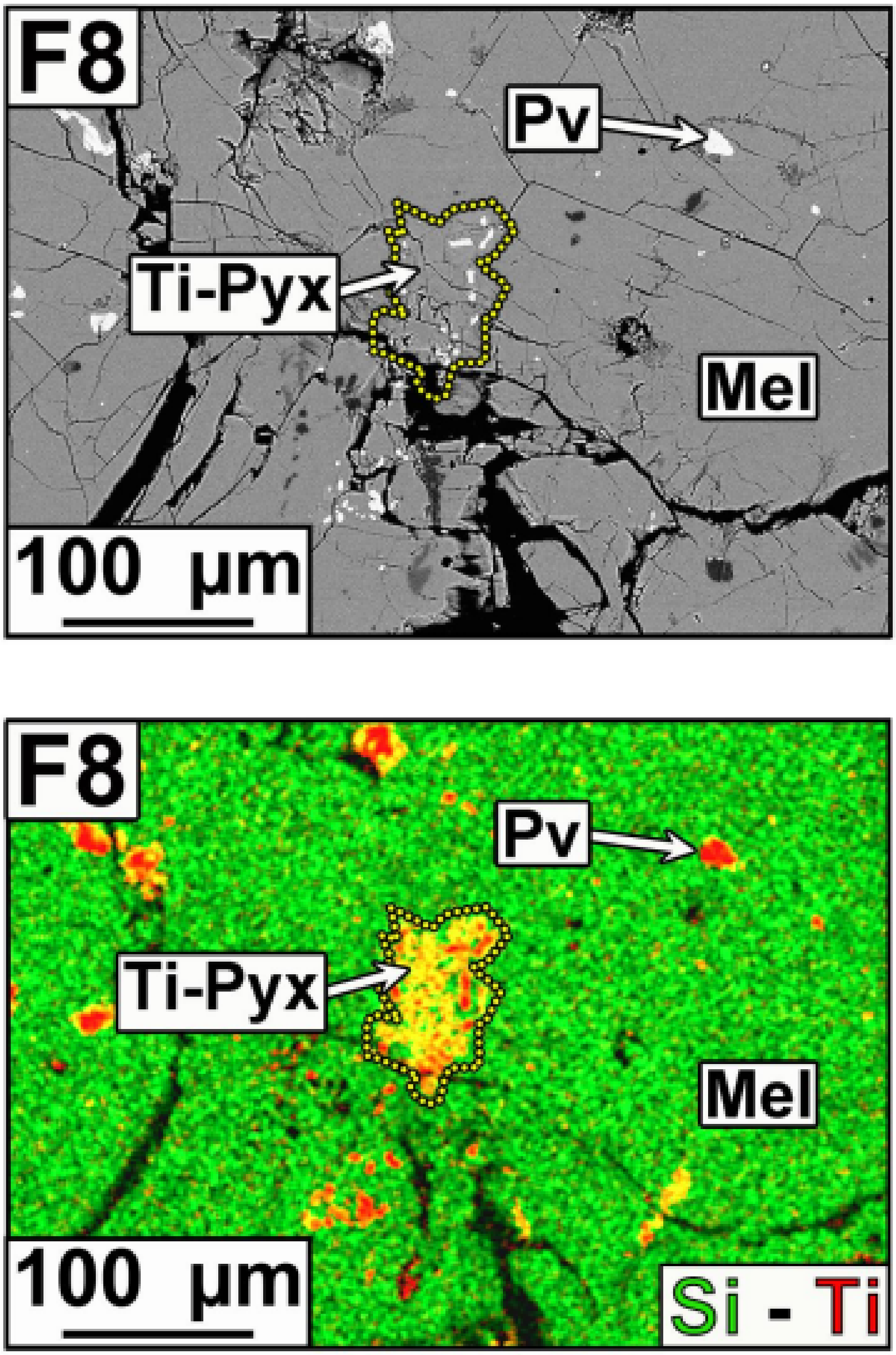

Figure 2.

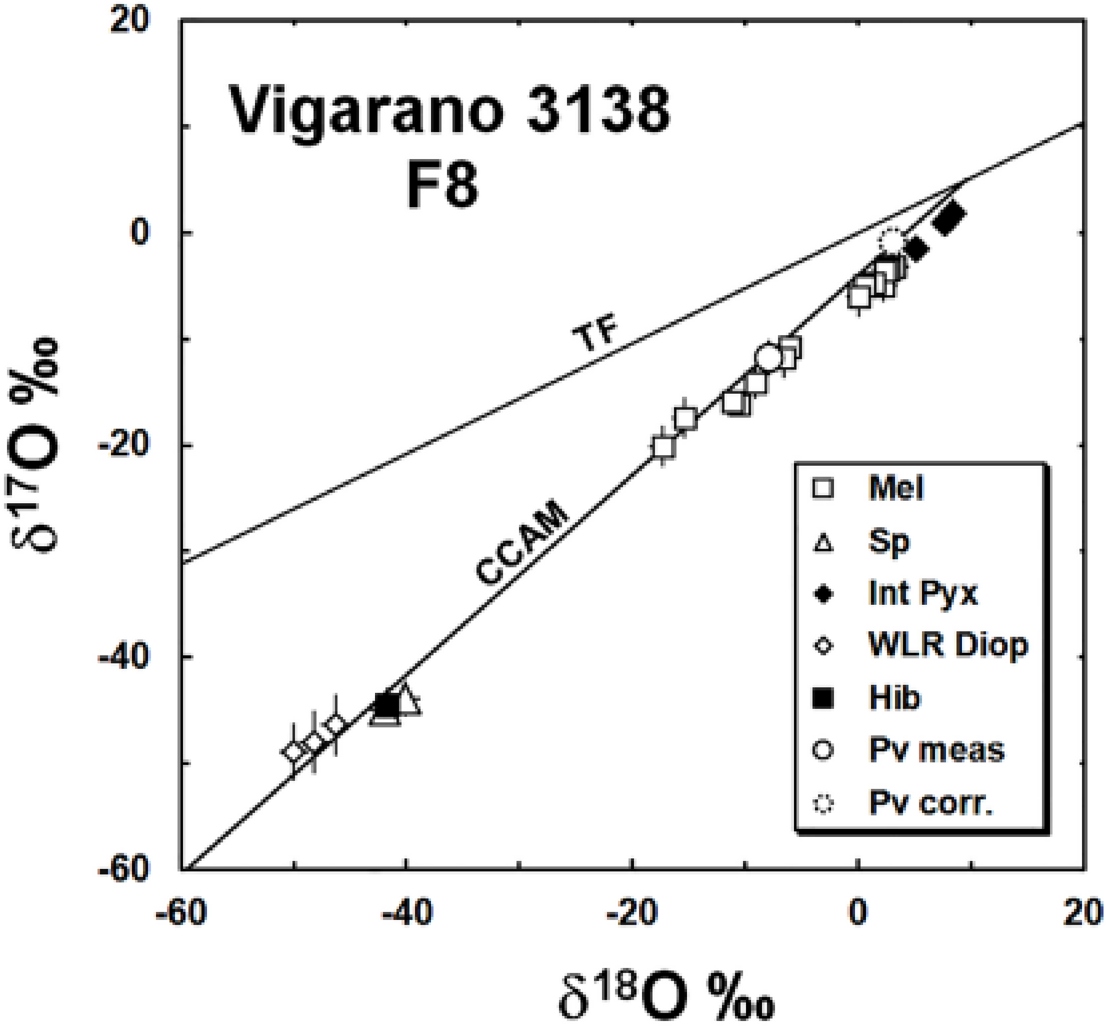
Vigarano 3138
F8
TF
CCAM
Mel
Sp
Int Pyx
WLR Diop
Hib
Pv meas
Pv corr.
20
0
-20
-40
-60
-60
-40
-20
0
20
δ17O ‰
δ18O ‰

Figure 3.

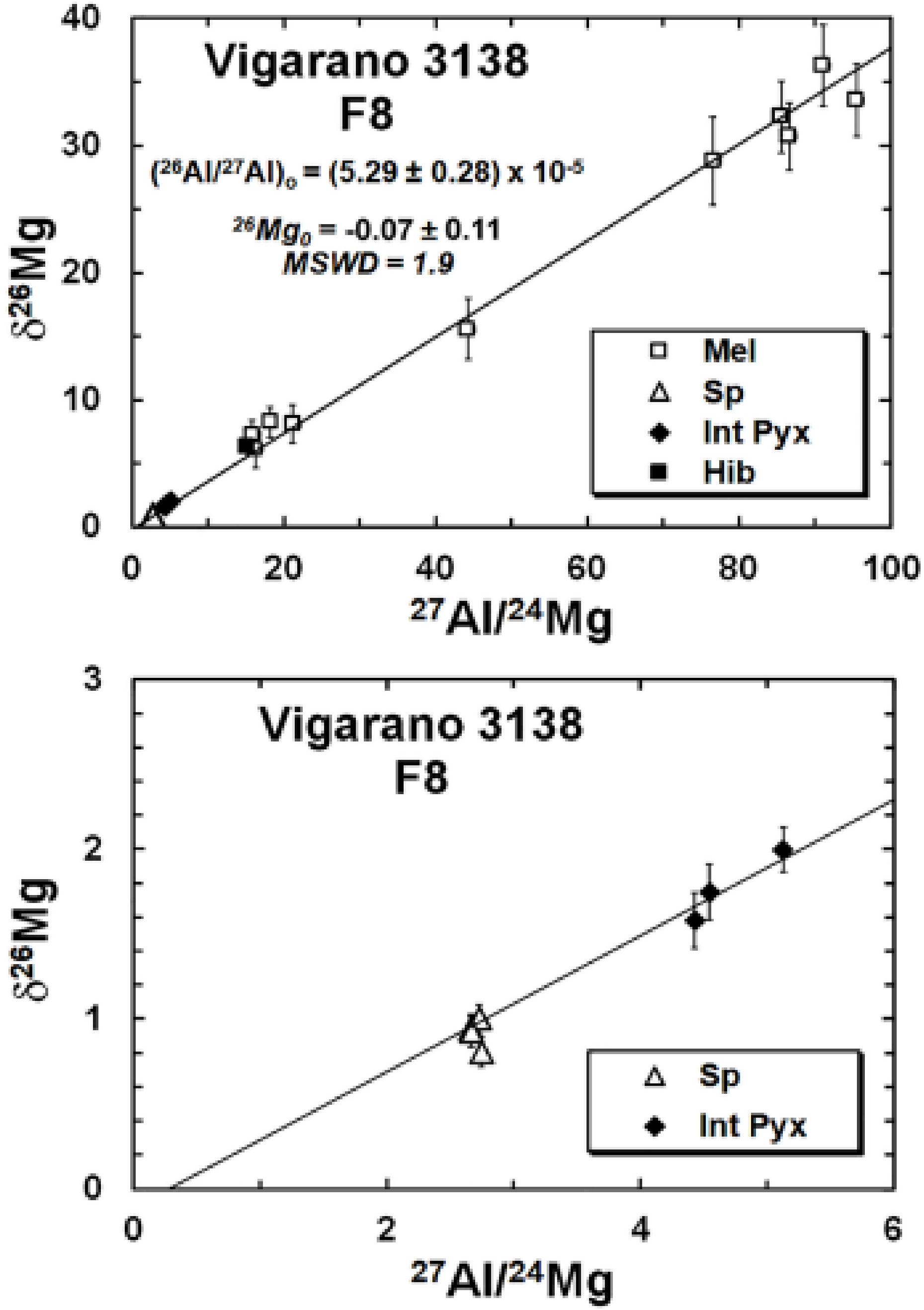
Vigarano 3138
F8
$(^{26}Al/^{27}Al)_o = (5.29 \pm 0.28) \times 10^{-5}$
$^{26}Mg_0 = -0.07 \pm 0.11$
MSWD = 1.9
Mel
Sp
Int Pyx
Hib
$\delta^{26}Mg$
$^{27}Al/^{24}Mg$
0
10
20
30
40
0
20
40
60
80
100
Vigarano 3138
F8
Sp
Int Pyx
$\delta^{26}Mg$
$^{27}Al/^{24}Mg$
0
1
2
3
0
2
4
6

Figure 4.

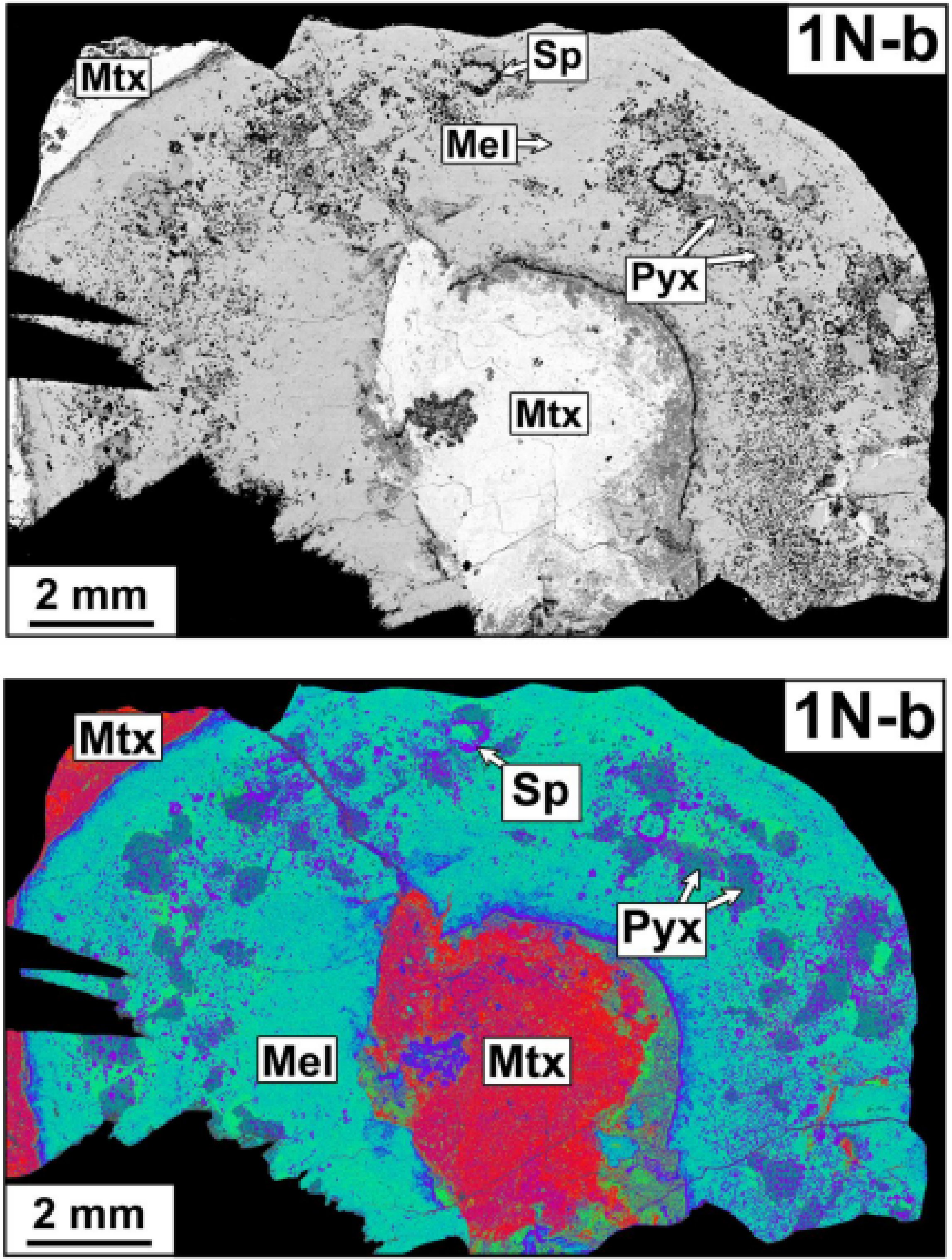

Figure 5.

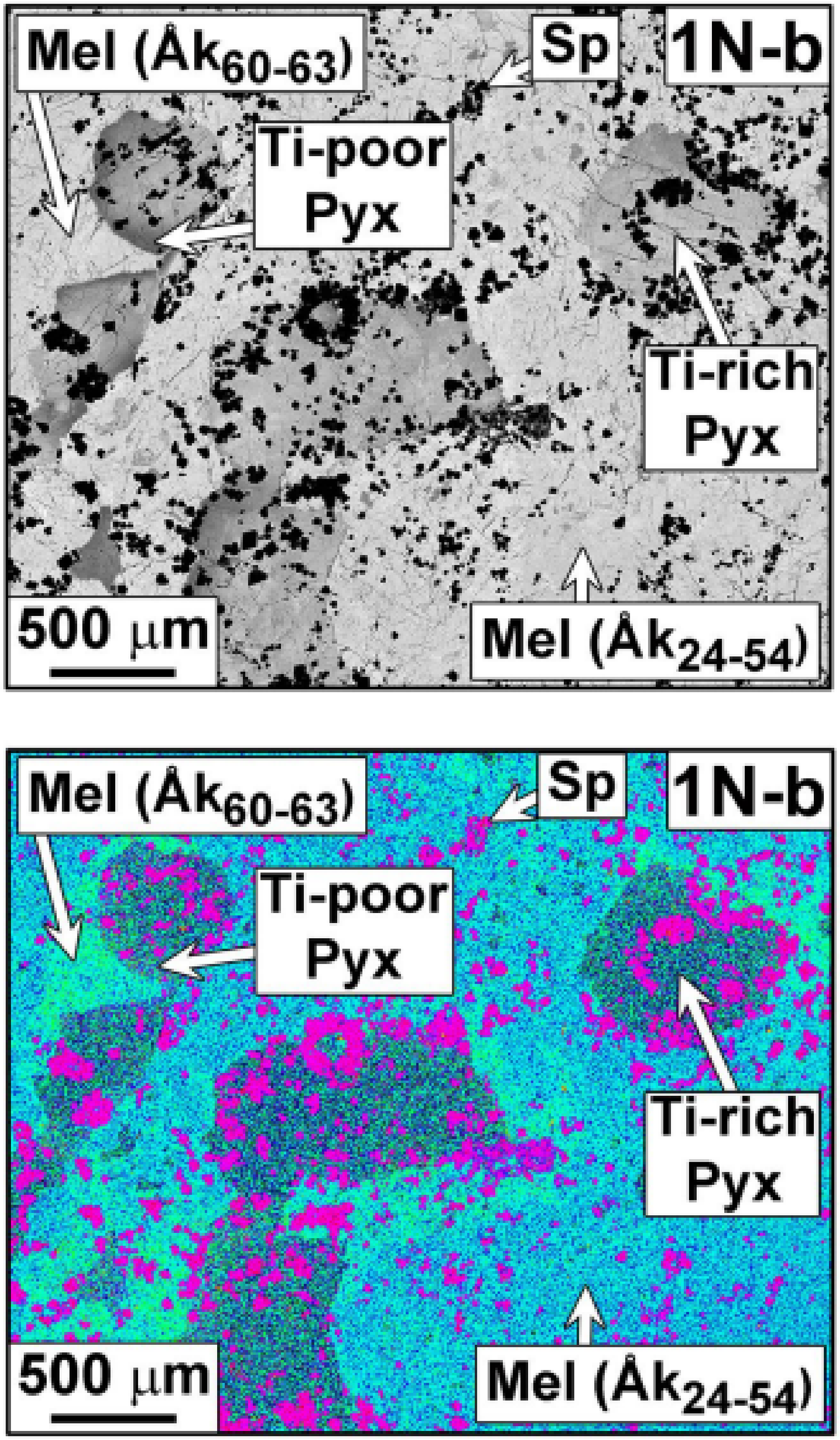
Mel (Åk60-63)
Sp
1N-b
Ti-poor Pyx
Ti-rich Pyx
500 μm
Mel (Åk24-54)
Mel (Åk60-63)
Sp
1N-b
Ti-poor Pyx
Ti-rich Pyx
500 μm
Mel (Åk24-54)

Figure 6.

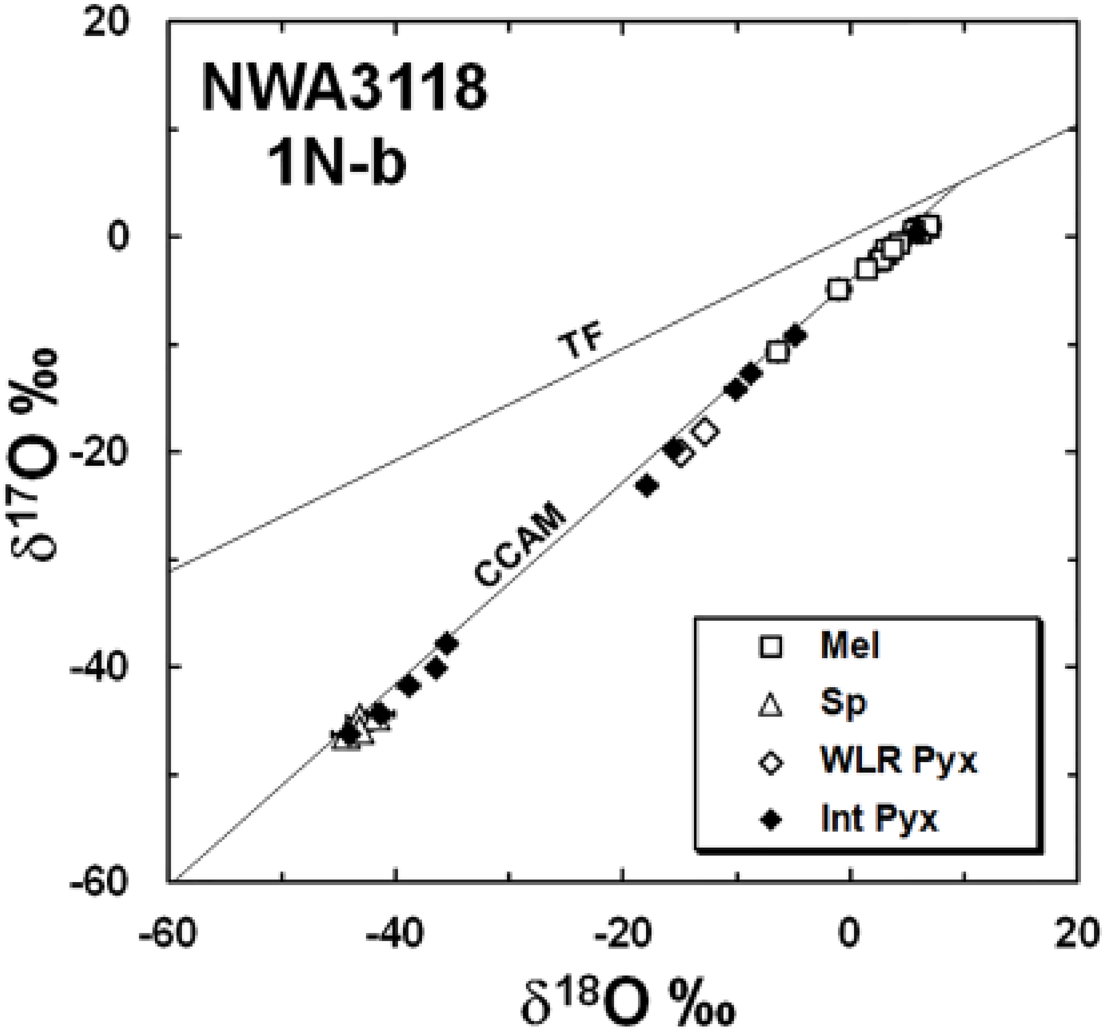
NWA3118
1N-b
TF
CCAM
Mel
Sp
WLR Pyx
Int Pyx
δ17O ‰
δ18O ‰
20
0
-20
-40
-60
-60
-40
-20
0
20

Figure 7.

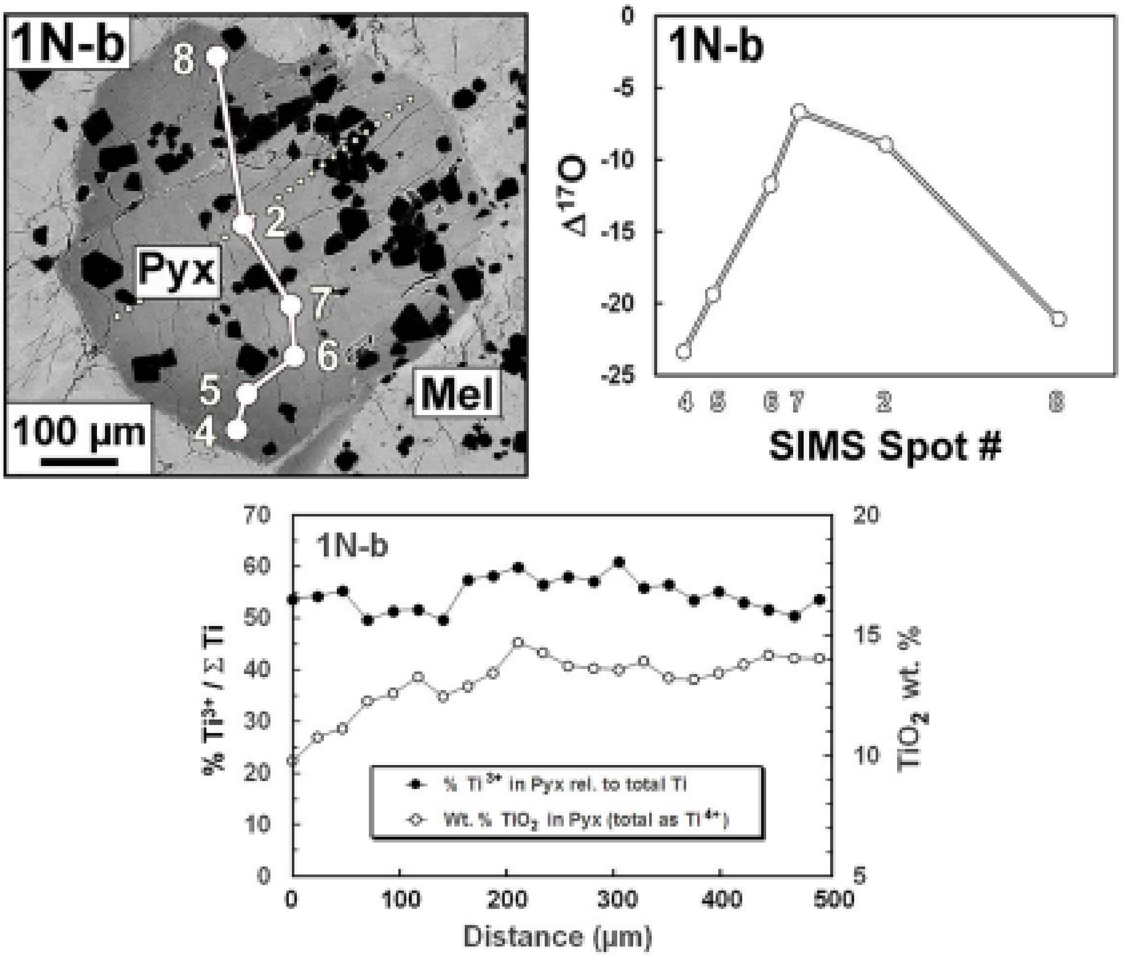
1N-b
8
2
7
6
5
4
Pyx
Mel
100 µm
1N-b
0
-5
-10
-15
-20
-25
$\Delta^{17}O$
4 5 6 7 2 8
SIMS Spot #
1N-b
70
60
50
40
30
20
10
0
% Ti^{3+} / Σ Ti
20
15
10
5
TiO_2 wt. %
% Ti^{3+} in Pyx rel. to total Ti
Wt. % TiO_2 in Pyx (total as Ti^{4+})
0
100
200
300
400
500
Distance (µm)

Figure 8.

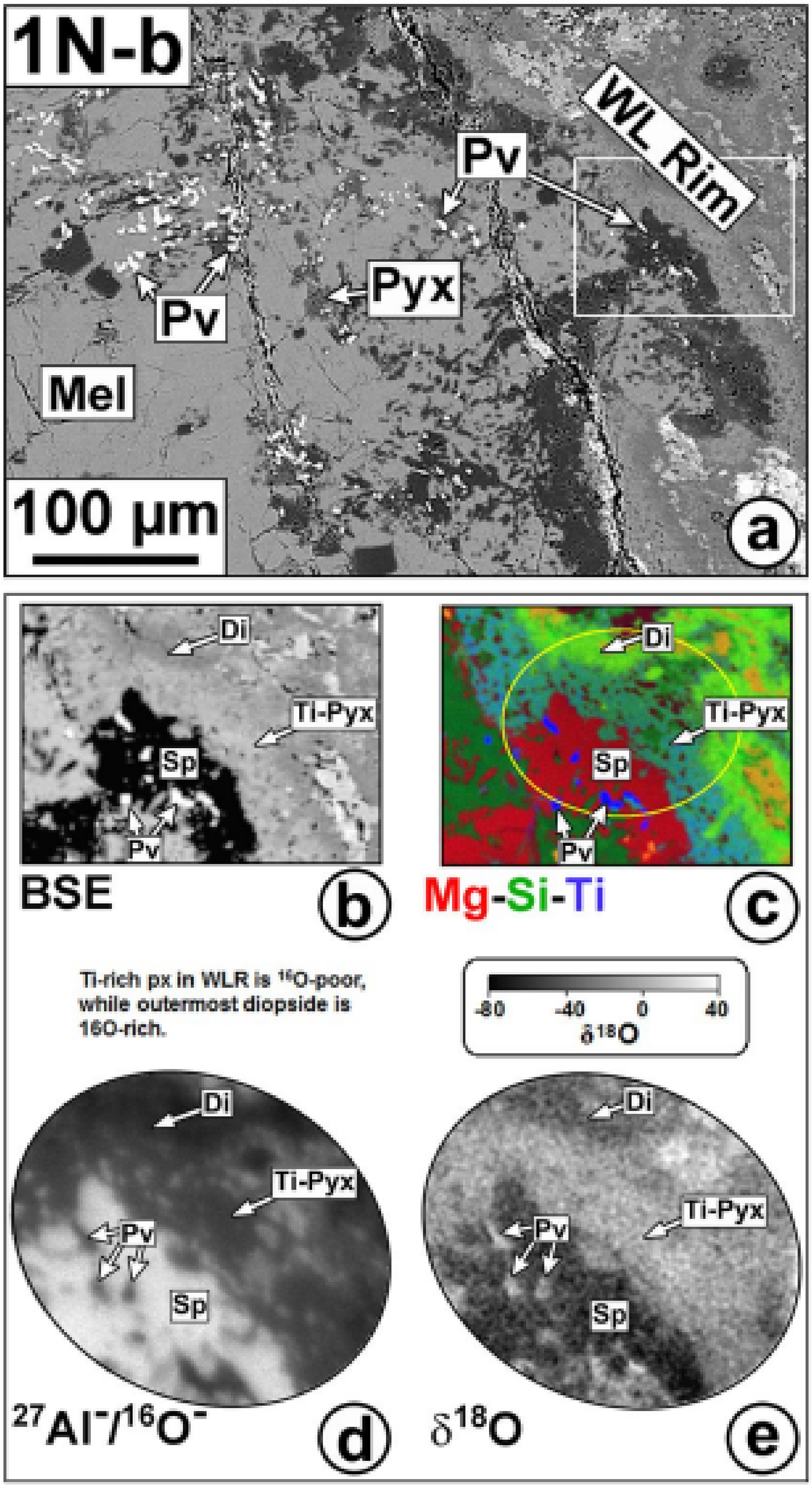

Ti-rich px in WLR is ^{16}O-poor, while outermost diopside is 16O-rich.

Figure 9.

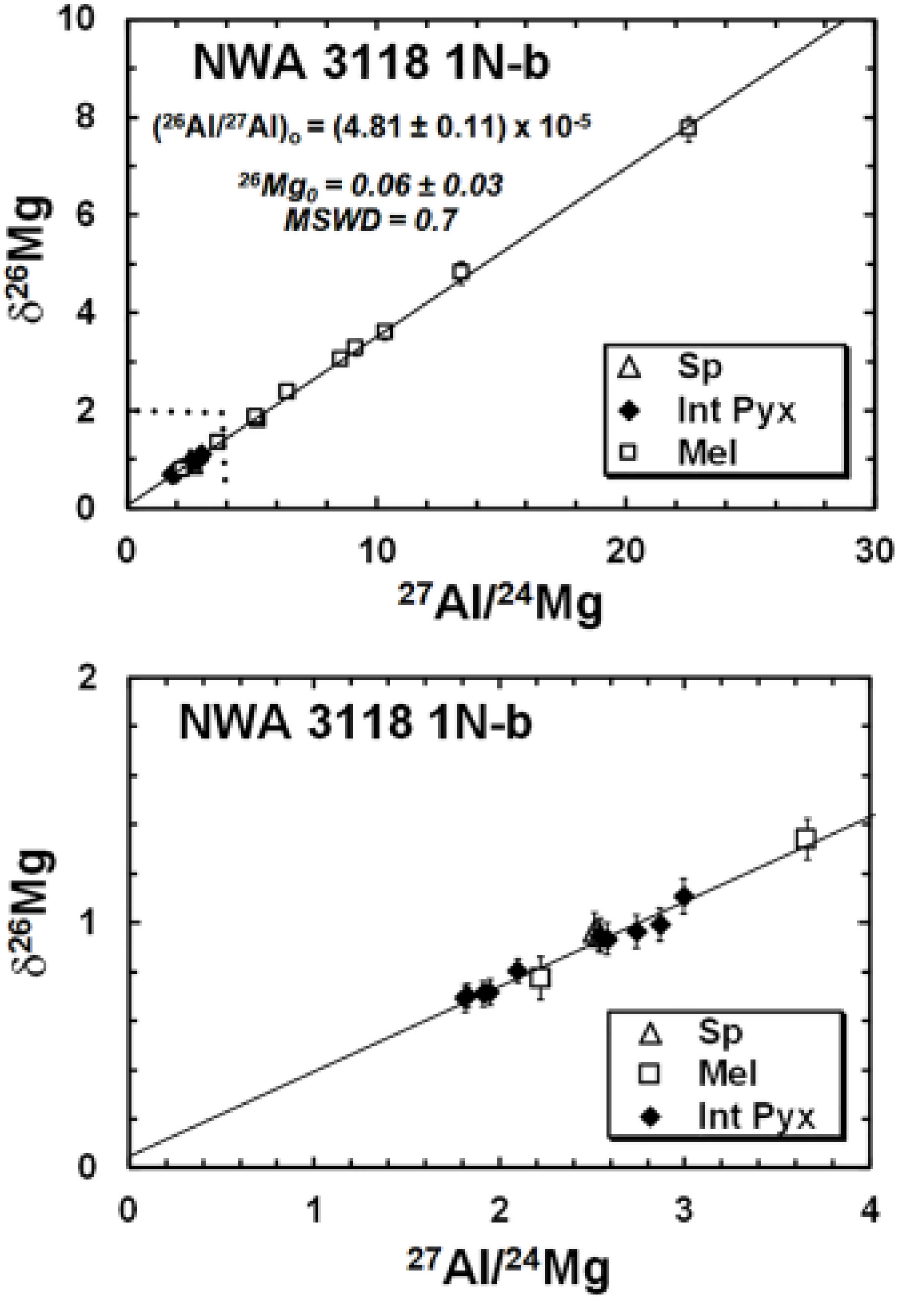
NWA 3118 1N-b
$(^{26}Al/^{27}Al)_o = (4.81 \pm 0.11) \times 10^{-5}$
$^{26}Mg_0 = 0.06 \pm 0.03$
MSWD = 0.7
Sp
Int Pyx
Mel
$\delta^{26}Mg$
$^{27}Al/^{24}Mg$
0
2
4
6
8
10
0
10
20
30
NWA 3118 1N-b
Sp
Mel
Int Pyx
$\delta^{26}Mg$
$^{27}Al/^{24}Mg$
0
1
2
0
1
2
3
4

Figure 10.

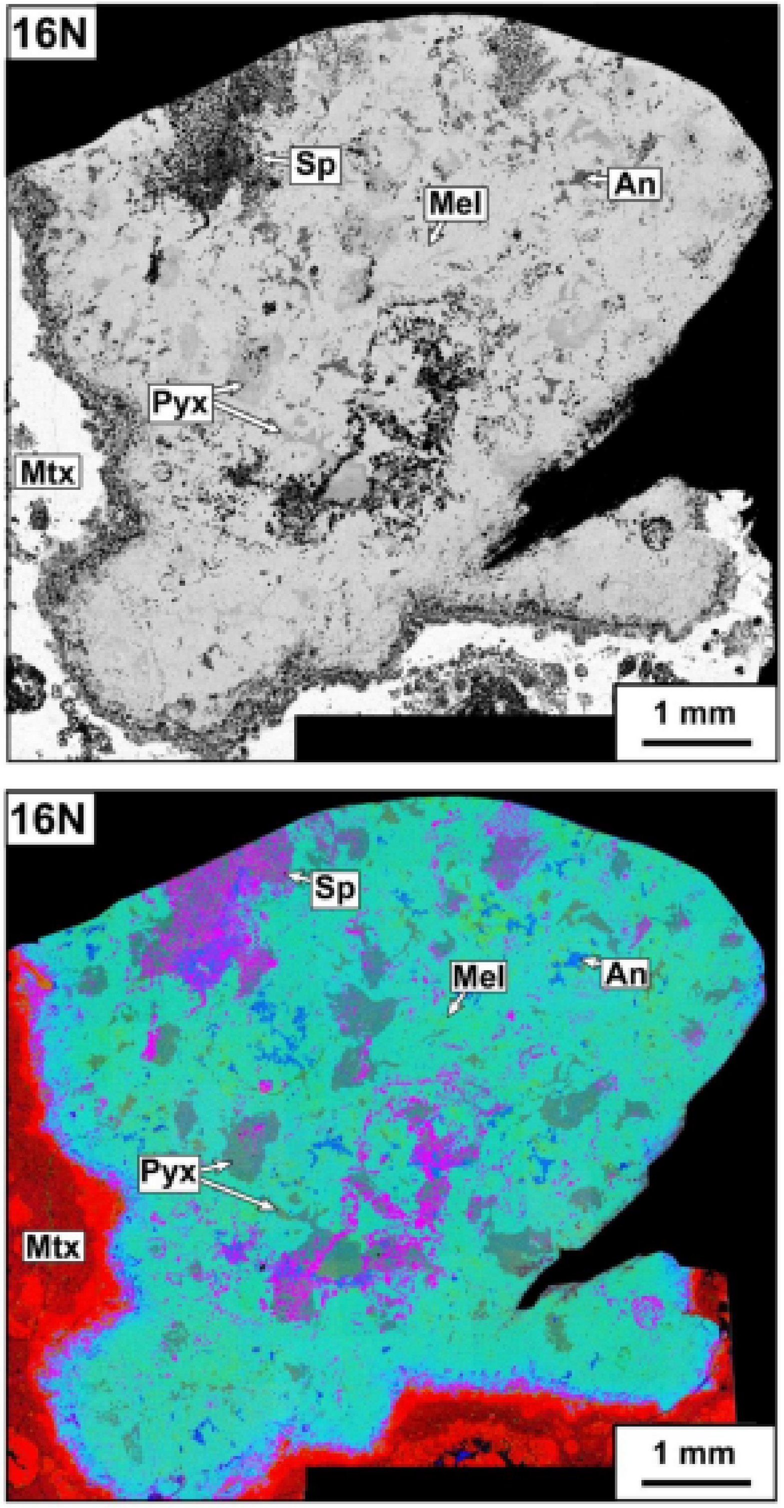

Figure 11.

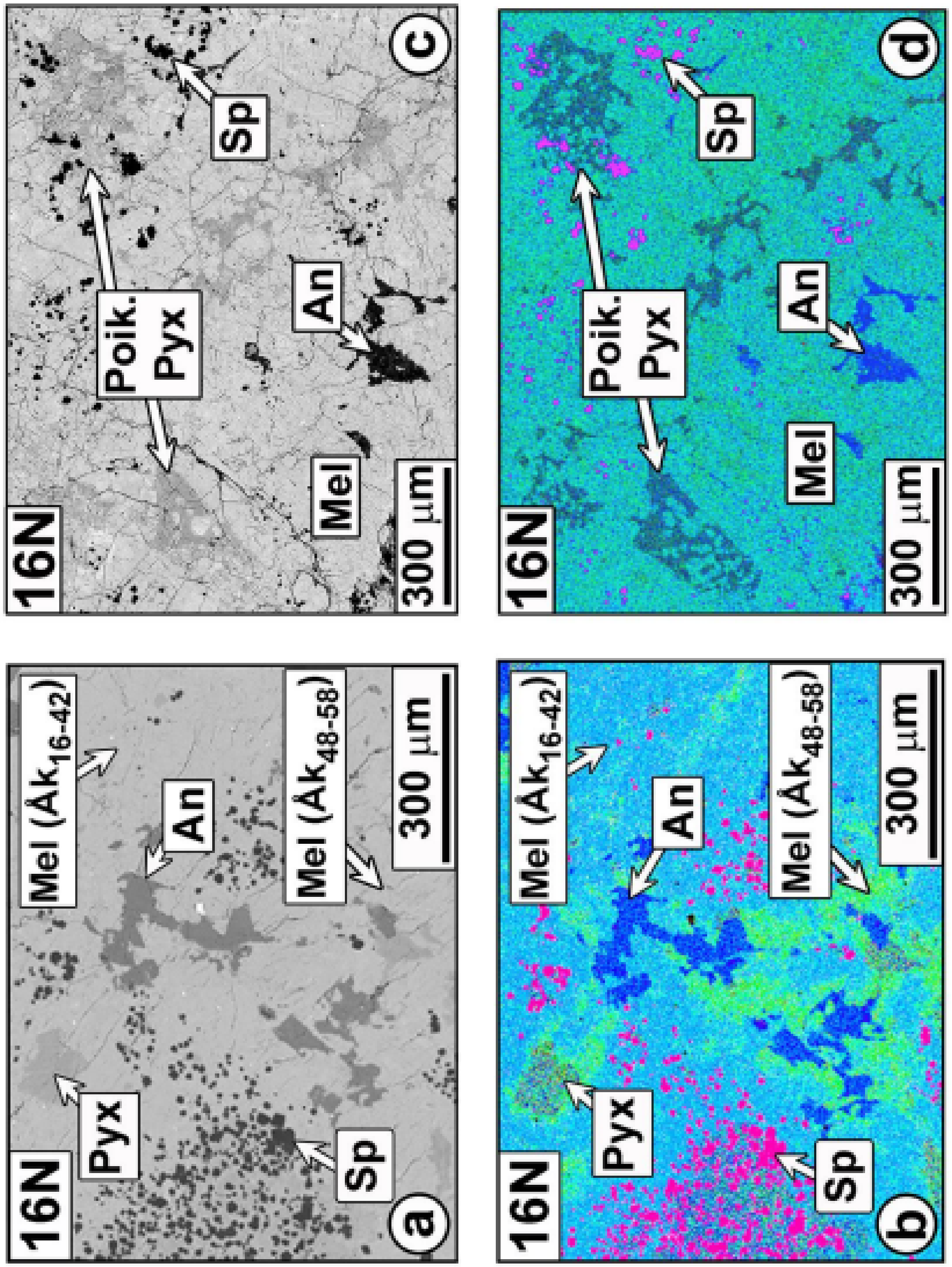

Figure 12.

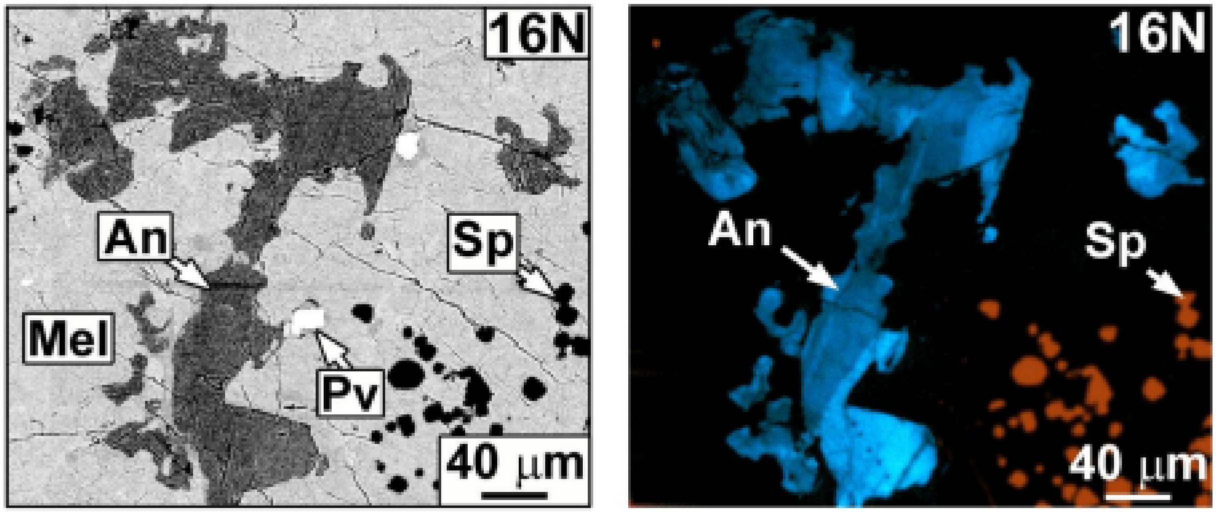

Figure 13.

Figure 14.

Figure 15.

Figure 16.

Figure 17.

Figure 18.

Figure 19.

Figure 20.

Figure 21.

Figure 22.

Figure 23.

Figure 24.

Figure 25.

Figure 26.

Figure 27.

Figure 28.

Figure 29.

Figure 30.

Figure 31.